

**Study of Photoionization and Dissociation
Dynamics of the Fullerene C₆₀**

**Bhim Prasad Kafle
Doctor of Philosophy**

**Department of Structural Molecular Science
School of Physical Science
The Graduate University for Advanced Studies
2007**

Acknowledgements

I would like to express the gratitude to Prof. Dr. Koichiro Mitsuke, associate professor of Graduate University for Advanced Studies and IMS, for his valuable and creative guidance for this research. I would like to thank Dr. Hideki Katayanagi for his continuous help during experiments and data analysis, and also other members of the Mitsuke group for their support during the course of my experiments. Special thank is due to the members of the UVSOR facility of IMS for their help during the course of the experiments. I would like to thank to Prof. Kosugi, and other professors in IMS with whom I got opportunities to learn about theory and experimental techniques regarding my work. I am very grateful to Heiwa Nakajima Foundation (**HNF**) that provided me with a financial support during this study and also express appreciation for providing Honors Scholarship from Japan Student Services Organization (**JASSO**). This work was supported by national funds appropriated for special research projects of the Institute for Molecular Science, by Grants-in-Aids for Scientific Research (Grant Nos. 14340188, 18350016, and 17750023) from Ministry of Education, Science, Sports, and Culture, Japan, and a grant for Scientific research from Research Foundation for Opto-Science and Technology.

Table of Contents:

Title of the thesis	i
Acknowledgements	ii
Contents	iii
List of abbreviations.....	v
Abstract.....	vi
Chapter 1	
1 General Introduction	1
1.1 Photoabsorption/ionization cross section of C_{60} in gas phase.....	6
1.2 Photodissociation dynamics of the fullerenes	8
References	13
Chapter 2	
2 Basic theory of photoabsorption by an atom or molecule	16
2.1 The absorption line	16
2.2 Photoabsorption cross section and oscillator strength	17
References	19
Chapter 3	
3 Experimental section.....	20
3.1 Overview	20
3.2 Synchrotron radiation and Monochromator	20
3.3 Experimental chamber and vacuum system.....	23
3.4 Experimental procedure and data acquisition system.....	23
References.....	25
Chapter 4	
4 Absolute Total Photoionization Cross Section of C_{60} in the extreme UV.....	29

4.1 Introduction	29
4.2 Methodology	31
4.3 Results and discussion	35
4.3.1 Photoionization cross section	35
4.3.2 Photoabsorption oscillator strength	36
4.4 Conclusions	40
References	41
Chapter 5	
5 A Design of Photofragment Imaging Apparatus for Measuring Momentum Distributions.	
5.1 Introduction	52
5.2 Basic concept and design optimized by simulations	54
5.3 Results	56
5.4 Conclusions	40
References	58
Chapter 6	
Summary of thesis	63
References	66
Appendixes	68
Appendix 1.....	68
Appendix 2.....	70
List of Publications	73

目次

iii ページ

誤 : Contents..... iii

正 : Table of Contents..... iii

誤 : 2 Basic theory of photoabsorption by an atom or molecule.....16

正 : 2 Basic theory of photoabsorption by an atom or molecule.....14

誤 : 2.1 The absorption line.....16

正 : 2.1 The absorption line.....14

誤 : 2.2 Photoabsorption cross section and oscillator strength.....17

正 : 2.2 Photoabsorption cross section and oscillator strength.....15

誤 : References.....19

正 : References.....18

誤 : 3 Experimental section.....20

正 : 3 Experiment.....19

誤 : 3.1 Overview.....20

正 : 3.1 Overview.....19

誤 : 3.3 Experimental chamber and vacuum system.....23

正 : 3.3 Experimental chamber and vacuum system.....22誤 : Absolute Total Photoionization Cross Section of C₆₀ in the extreme UV.....29正 : Absolute Total Photoionization Cross Section of C₆₀ in the Range of 25-120eV.....28

iv ページ

誤 : 4.1 Introduction.....29

正 : 4.1 Introduction.....28

誤 : 4.2 Methodology.....31

正 : 4.2 Methodology.....30

誤 : 4.3 Results and Discussion.....35

正 : 4.3 Results and Discussion.....32

誤 : 4.3.1 Photoionization cross section.....35

正 : 4.3.1 Photoionization cross section.....32

誤 : 4.3.2 Photoabsorption oscillator strength.....36

正 : 4.3.2 Photoabsorption oscillator strength.....34

誤 : 4.4 Conclusions.....40

正 : 4.4 Conclusion.....38

誤 : References41

正 : References39

誤 : A Design of Photofragment Imaging Apparatus for Measuring Momentum Distributions.....52

正 : Photofragment Imaging Apparatus for Measuring Momentum Distributions in Dissociative Photoionization of Fullerenes.....48

誤 : 5.1 Introduction.....52

正 : 5.1 Introduction.....48

誤 : 5.2 Basic concept and design optimized by simulations54

正 : 5.2 Basic Concept and Design Optimized by Simulations50

誤 : 5.3 Results.....56

正 : 5.3 Results.....52

誤 : 5.4 Conclusions.....40

正 : 5.4 Conclusions.....54

誤 : References58

正 : References56

誤 : Summary of the Thesis63

正 : Summary of the Thesis62

誤 : Appendixes68

正 : Appendixes67

誤 : Appendix 168

正 : Appendix 167

List of abbreviations

synchrotron radiation, **SR**

extreme ultraviolet, **EUV**

time-of-flight spectrometer, **TOF spectrometer**

absolute total photoionization cross section, $\sigma_{\text{abs,I}}$

absolute photoabsorption cross section, $\sigma_{\text{abs,A}}$

photon energy, $h\nu$

mass-to-charge ratio, m/z

microchannel plate, **MCP**

absolute partial cross section for the formation of singly charged C_{60} ion, $\sigma_{\text{abs}(+)}$

absolute partial cross section for the formation of doubly charged C_{60} ion, $\sigma_{\text{abs}(2+)}$

absolute partial cross section for the formation of triply charged C_{60} ion, $\sigma_{\text{abs}(3+)}$

absolute overall detection efficiency of the apparatus, η_{abs}

oscillator strength distribution, df/dE

photoabsorption oscillator strength, f

Thomas-Kuhn-Reiche sum rule, **TKR sum rule**

potential energy surface, **PES**

resonance-enhanced multiphoton ionization, **REMPI**

position sensitive detector, **PSD**

Abstract

In the present thesis, the results of the study on the absolute total photoionization cross section $\sigma_{\text{abs,I}}$ of gaseous C_{60} in the photon energy $h\nu$ range from 25 to 120 eV are presented. The measurements are carried out by using photoionization mass spectrometry in combination with synchrotron radiation. Absolute partial cross sections $\sigma_{\text{abs}}(z^+)$ ($z = 1-3$) for the formation of the ions in a charge state z from C_{60} were evaluated by considering the absolute detection efficiencies of photoions in different charge states. Then the absolute total photoionization cross section ($\sigma_{\text{abs,I}}$) was obtained by summing up all of the $\sigma_{\text{abs}}(z^+)$. Moreover, the present $\sigma_{\text{abs,I}}$ curve was combined with the photoabsorption cross section curves of C_{60} at $h\nu = 3.5 - 26$ eV in the literature, after appropriate alterations of the vapor pressure are taken into account. The oscillator strengths are computed from the composite curve to be 178.5 and 230.5 for the $h\nu$ ranges from 3.5 to 40.8 eV and from 3.5 to 119 eV, respectively. These oscillator strengths agree well with those expected from the Thomas-Kuhn-Reiche sum rule and 60 times the photoabsorption cross section of a carbon atom. Moreover, the present $\sigma_{\text{abs,I}}$ curve behaves similarly to the relative photoionization cross section curve reported by Reinköster *et al.* [J. Phys. B, 37(2004) 2135].

When a fullerene, in particular C_{60} molecule, absorbs a photon of energy ~ 41 eV or above, a highly excited ion of C_{60} is produced and then dissociates into smaller ionic and neutral fragments. In this thesis, description is also made on a design of a new version of photofragment imaging spectrometer, which will be applied to observe the momentum distributions of ionic fragments from large molecules, clusters, and fullerenes. The apparatus consists of several components: circular electrodes, a time-of-flight drift tube, a potential-switchable mass gate,

ion reflector, and a position sensitive detector. The velocity focusing lens system of Eppink-Parker type [Eppink and Parker, Rev. Sci. Instrum. **68**, 3477(1997)] realizes high resolution of the photofragment images. Moreover, the mass gate is incorporated inside the tube in order to separate fragment ions with a particular cluster size (e.g. C_{58}^+) from those with other sizes (e.g. C_{60}^+ , and C_{56}^+). The optimum arrangement and dimensions of the components are determined from the results of ion trajectories of C_{56}^+ , C_{58}^+ and C_{60}^+ simulated by using the SIMION software. The calculated images of C_{58}^+ ions show that kinetic-energy resolution of 10 meV is achievable. It is expected that useful information on reaction mechanism of highly-excited fullerene ions can be derived from the momentum distributions of the fragments.

Chapter 1

1 General Introduction

Understanding excitation and chemical reaction dynamics of molecules is one of the most important goals of chemical physics. For achieving these goals, several modern spectroscopic techniques such as laser spectroscopy, photoabsorption spectroscopy, photoionization mass spectrometry, momentum imaging spectrometry, have been developed. These spectroscopic methods are closely related to the interaction of molecules with electromagnetic radiation, and can extensively explore molecular properties in the energy range from microwave to X-ray. For example, the rotational transition of molecules typically occurs by absorption and emission of radiation in the microwave region, and the electronic transition from an inner-shell molecular orbital is caused by absorption of radiation in the X-ray region.

As described in the textbook of Samson [1] and the review of Hatano [2] the energy region from ~ 12 eV to ~ 6 keV (the wavelength region from 0.2 nm to 100 nm) in the electromagnetic spectrum is categorized as the extreme UV (EUV) region. The EUV radiation which is emitted from the sun is promptly absorbed by the uppermost atmosphere and eventually molecular ions and electrons densely exist as plasma. Therefore, the importance of photochemistry in the extreme UV region has attracted a growing interest from the view point of atmospheric chemistry.

In particular, studies on photoexcitation and decay dynamics of molecules in this energy region are significantly important since both photoabsorption and photoionization cross sections take large values in the EUV region for almost all molecules [2]. The study of interaction between a molecule and synchrotron radiation in the EUV region can provide us with valuable spectroscopic information,

particularly, in molecular photoionization and photodissociation processes. Since almost all molecules have the lowest ionization potential below 20 eV, their photoabsorption cross section curves show continuous behavior due to direct photoionization in the EUV region. In addition, photoabsorption spectra, in this energy range, are greatly diversified by excitation into neutral quasi-discrete states. Such states have an internal energy larger than that of the lowest ionization potential and are often referred to as superexcited states [2-5].

Photoabsorption and photoionization cross sections are fundamental spectroscopic properties of isolated molecules. Determining their magnitudes as a function of photon energy gives the energy dependent transition probability or oscillator strength. Oscillator strength is a dimensionless parameter to express the strength of transition (if an electron bound to a nuclear framework possesses perfect oscillating properties following a harmonic motion then from the classical theory the excitation probability of that electron can be expected to have an oscillator strength of unity). As stated in the former paragraph, major parts of both photoabsorption and photoionization cross section spectrum for almost all molecules lie in the EUV region [2]. Actually many molecules have maximum oscillator strength in the energy range between 10 and 30 eV.

One of the remarkable discoveries in the late 20th century was the fullerene, the third allotrope of carbon after diamond and graphite. The closed form of these molecules is built up by carbon atoms having 12 pentagons and a varying number of hexagons. The C₆₀ fullerene with a structure of truncated icosahedron is a good example of this novel form of carbon. Because it is an exceptionally stable and symmetric cluster, C₆₀ has received much attention of scientists in many fields of

expertise. Indeed, there has been speculation on the possible chemical and industrial uses of C_{60} [6], and on its importance in astrophysical environments [7-8]. In this prospect endohedral metallofullerenes (fullerenes with metal atom encapsulated) has already been prepared successfully. These compounds are particularly interesting because the electron transfer from the encaged metal atom to the carbon cage is known to occur and this substantially alters electronic and magnetic properties of the fullerenes [9]. Superconductivity was discovered at high temperatures in the alkali metal fullerides, K_3C_{60} (at critical temperature $T_C = 19$ K [10]) and Rb_3C_{60} [11]. Moreover, there has been genuine attempts to produce C_{60} based solar cells [12-14].

In the spectroscopic point of view, the fullerenes in general, and C_{60} in particular, demonstrate unique photoabsorption and ionization properties. Moreover, observing the intrinsic behavior of such a highly symmetric molecule C_{60} after ejecting one or more electrons by photon impact could give us great insight into the single and multiple-photoionization processes and nature of dissociation of other clusters. Actually, a relative curve of the photoionization cross section from the ionization threshold up to 280 eV (the carbon K-edge) has already been recorded [15-22] and revealed several peculiar phenomena. For example a strong peak lying at $h\nu \sim 20$ eV with an FWHM of ~ 10 eV was demonstrated in the ion yield curve measured by Hertel et al.[15] from ionization threshold (7.6 eV) to 35 eV. They ascribed this peak to a giant plasmon resonance, which was also observed in the yield curve of C_{70}^+ from C_{70} . The plasmon resonance in C_{60} has been accounted for by that 240 valence electrons are delocalized over the surface but confined in a thickness of single carbon atom in the radial direction. Moreover, a markedly higher ratio of the yield of multiply charged ions to singly charged ions of C_{60} in comparison to the

corresponding ratio for small molecules was observed, at particular photon energies [20-22].

Now, photoionization (or photoabsorption) cross section in an absolute scale is still to be settled because of several difficulties to be encountered for such quantitative experiment (discussion on this issue is made in the successive section). On the other hand, when C_{60} is exposed to the photon of energy ~ 41 eV or above the highly excited C_{60} parent ion undergoes fragmentation mainly by sequential loss of C_2 unit. A few experimental efforts [23-25] have been made in order to realize whether the fission process by losing C_4 , or $C_6\dots$, is also a possible channel, although their experimental technique could not provide direct evidence to support to this channel. Therefore, in this thesis work, I devoted in the following two major directions of study, for tackling such genuine questions:

(I) Determination of absolute total photoionization cross section of C_{60} excited with synchrotron radiation in the EUV region.

(II) Design of the photofragment imaging apparatus for measuring momentum distributions of cationic fragments produced after dissociation of C_{60} photoions.

1.1 Photoabsorption and photoionization cross sections of C_{60}

In order to understand the excitation and ionization dynamics of fullerenes, the relative photoionization cross section of C_{60} have been measured by means of mass spectrometry in the extreme UV region [15-22]. From these studies it has been revealed that the cross section curve shows several resonant peaks at photon energy below $h\nu \sim 50$ eV, reflecting the molecular character of C_{60} in its valence photoionization. Hertel *et al.* [15] showed that the yield curve of C_{60}^+ produced from C_{60} shows a markedly strong peak lying at $h\nu \sim 20$ eV due to collective excitation of

240 valence electrons. On the other hand, spectrum from recent studies show [18-19] fine peaks at $h\nu = 26$ and 34 eV and a flat area ranging from 40 to 50 eV in the yield curve, which have been ascribed to shape resonance. It is worthwhile to clarify that we have observed these features (fine peaks at $h\nu = 26$ and 34 eV) repeatedly even after normalizing our photoion counts to the photon flux measured using gold mesh. Thus these structures are not artifact as claimed by Scully *et al.* [26]. Moreover, in 2007, we have reinvested the ion yield curves of singly- and multiply-charged ions, mainly, C_{60}^{z+} ($z = 1 - 3$) [22]. In this study, close evaluation of the relative detection efficiency η of the MCP detector for each charged species produced from C_{60} was made and the percentage of the second order light in SR radiation was taken into account. Then the derived spectrum of total cross section was in accordance with the relative photoabsorption cross section of C_{60} [24]. It was also, explicitly, demonstrated that the ratios $\sigma(60,2+)/\sigma(60,+)$ and $\sigma(60,3+)/\sigma(60,+)$ between the partial cross sections for double and single photoionization of C_{60} and triple and single photoionization of C_{60} , respectively, increase with increasing photon energy and asymptotically reaches upto 0.78 and 0.14 , respectively [22]. The above observations are explained as that the excess internal energy is transmitted so rapidly among enormous vibrational degrees of freedom (174 vibrational degrees of freedom in the case of C_{60}) that unimolecular reactions, such as direct dissociation, predissociation, or coulomb explosion, are significantly suppressed and the lifetime of the parent ions is elongated beyond the order of a millisecond [19,22].

As stated in the previous section, to obtain the absolute photoionization or photoabsorption cross section curve of C_{60} is another important issue which still remains to be established. Actually there exist only a few experimental works on the measurements of absolute total photoionization cross section ($\sigma_{\text{abs,t}}$) and absolute

photoabsorption cross section ($\sigma_{\text{abs,A}}$) of C_{60} in the extreme UV region [16,20,27-31]. However, even among these few measurements, the cross section values differ severely from each others in the overlapping region of energy. From close inspection of available data in literatures on $\sigma_{\text{abs,I}}$ and $\sigma_{\text{abs,A}}$, we noticed that the most dubious parameter was vapor pressure, since the vapor pressure data which have been utilized to predict the cross section values varies widely by a factor of 1.5 to 6 at a particular temperature [32-35] (for example, the vapor pressure measured by Abrefah *et al.* [32] was given to be ~ 0.07 Pa and that measured by Jaensch and Kamke is 0.416 Pa at 500 °C).

In the present dissertation, first, $\sigma_{\text{abs,I}}$ of C_{60} at extreme UV region was evaluated on a basis of the latest detection efficiency (η) corrected data [22] of the relative partial cross sections for production of singly-, doubly-, and triply-charged ions. Then $\sigma_{\text{abs,I}}$ was combined with the previously published $\sigma_{\text{abs,A}}$ curves, after critically analyzing the vapor pressure data which were utilized in the literature, in order to derive the reliable curves of absolute cross sections over a wide energy range from 3.5 to 119 eV. From these curves, estimation of the oscillator strength has been made.

1.2 Photodissociation dynamics of the fullerenes

When a polyatomic molecule absorbs the light with an energy exceeding the dissociation threshold energy of its weakest bond, fragmentation can occur. The potential energy surface (PES) of the excited parent molecule determines the dynamics of this process, and consequently the branching ratios for fragmentation pathways and energy distribution in the photoproducts. Dissociation of the molecules is known to take place in two ways: direct and indirect dissociation [5,37]. In the case

of a direct dissociation the PES of the excited state is strongly repulsive along one or more coordinates yielding an extremely fast (< 10 fs) bond-breaking process, as shown in the Fig. (1.1a). In this dissociation process one may expect that a large fraction of the energy is released as translational energy. On the other hand, the indirect dissociation maybe the result of an excited state PES characterized by local well along the reaction coordinate as depicted in the Fig. (1.1b). The potential well acts like a “short-term waiting room” for the excited molecule to decay and it gives rise to pronounced structures in the absorption spectrum which reflect the energy spacing of the quasi-bound states supported by the potential well [37].

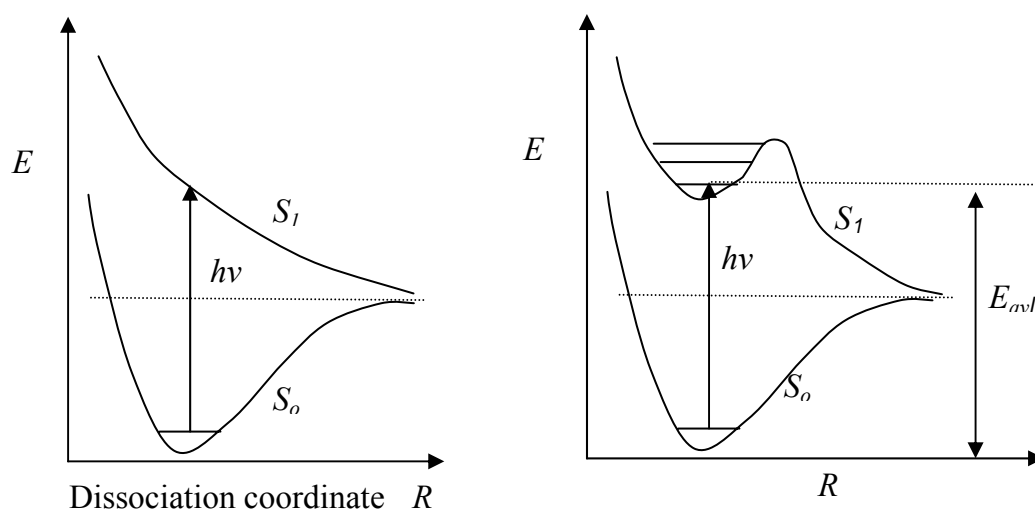
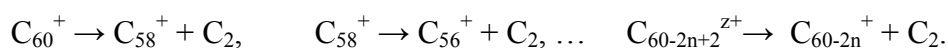


Fig. 1.1 Direct dissociation, left (a); and indirect dissociation (predissociation), right (b).

If we can visualize the motion of dissociating fragments in unimolecular reactions of energized isolated molecule, we will be able to achieve utmost understanding on the reaction dynamics involved. With such a prospect the photodissociation dynamics of various diatomic and polyatomic molecules has been studied theoretically and experimentally by utilizing various spectroscopic methods.

Photofragment translational spectroscopy in combination of TOF mass spectrometry is valuable in obtaining a fairly clear picture of the photodissociation process [38].

When fullerene C_{60} receives excess amount of energy through photoionization, primarily formed ions are known to undergo decomposition into fragment ions with even numbered carbon atoms. Measurements on the ion yield curves of the fragments C_{60-2n}^{z+} and C_{70-2n}^{z+} ($n \geq 1, z \geq 1$) produced by photoionization of solitary C_{60} and C_{70} , respectively, have been reported in the EUV region [20,23,39]. Comparison between the experimental results and theoretical calculations revealed that the supplied excess energy is statistically distributed among the internal degrees of freedom of the parent ions and C_2 units are ejected sequentially as follows [23,39]:



This conclusion was made on the basis of the findings that the experimentally observed ion yield curves and theoretically derived fractional abundance curves showed almost the same appearance energies for the formation of C_{60-2n}^{z+} ($n \geq 1$) [23,39]. The latter curves were derived by employing the RRKM theory to individual unimolecular reactions, $C_{60-2n+2}^{z+} \rightarrow C_{60-2n}^{z+} + C_2$. More reliable calculations of the rate constants of the consecutive reactions are seek before closer comparison between the two curves. For such calculations we should know precise values of the activation energies of the reactions, together with the vibrational spectra of the transition states.

On the other hand, as mentioned in the previous section, besides mechanism of sequential loss of C_2 unit from C_{60}^{z+} , a few groups [24,25] have (argued and) attempted to find whether single-step two-fragment fission



could also be a possible reaction path for the formation of C_{60-2n}^{z+} . The fragmentation pathways have been studied by measuring the average kinetic energy (KE) release in

the decomposition reaction of C_{60}^{z+} into C_{60-2n}^{z+} by means of (a) laser multiphoton ionization mass spectrometry of C_{60} [24] and (b) electron impact ionization mass spectrometry of C_{60} in conjunction with the ion deflection method [25]. However, their results on average KE release did not allow them to obtain conclusive evidence on whether such a mechanism takes part in. These unsolved problems induced us to develop a new spectrometer based on imaging technique in order to study the ionic fragments produced from C_{60}^{z+} and C_{70}^{z+} . In contrast to the conventional time-of-flight method, where kinetic energy release information is contained in the temporal structure in the arrival period of electrons or ions of a specific mass, the ion imaging technique extracts all information (kinetic energy and angular distributions) from the spatial appearance of the two-dimensional (2D) image.

However, in order to exploit the imaging method to its full potential one needs to improve the quality of the 2D image. The mapping of 3D distributions of charged particles onto the 2D detector is particularly dependent on the configuration of the electrodes generating the extracting electric field [40]. The three-element velocity focusing lens system of Eppink-Parker type [40] surely satisfies this condition and high kinetic energy resolution can be achieved on the photofragment images. We optimized a photofragment imaging apparatus based on this lens system by simulation using the SIMION software [41] to obtain a 2D-image of the 3D-velocity distributions of a desired fragment. In order to select a bunch of fragments having the same mass-to-charge ratio m/z we put a potential switcheable *mass gate* and an *ion reflector* inside the TOF tube. The assembly of three-element velocity focusing lens system of Eppink-Parker type in combination with the *mass gate* and *ion reflector* makes our apparatus unique.

In this dissertation I will show that, from the simulated trajectories of C_{60}^+ , C_{58}^+ , and C_{56}^+ , at initial kinetic energy of 0.1 eV, most of the trajectories of C_{58}^+ are found to pass through the ion reflector and reach the PSD. In contrast, the trajectories of C_{60}^+ and C_{56}^+ are reflected completely. Indeed, this observation provides direct evidence for exclusive imaging detection of C_{58}^+ by excluding C_{60}^+ and C_{56}^+ with the same kinetic energies. Furthermore, the image resolution of this apparatus will be determined by presenting individual images on the PSD for the C_{58}^+ ions with only a very small kinetic energy difference of about 10 meV.

In experiment, this observed 2D image of the 3D distribution of an ionic fragment can easily be processed for deriving the translational energy distribution of a desired fragment with a very good energy resolution. Therefore, it is likely that, from the translational energy distribution, we can reveal (a) which reaction mechanisms are dominant in the above photodissociation process and also possibly can observe (b) whether potential barrier exists along the reaction coordinate.

References

- [1] J. A. R. Samson, In: *Techniques of Vacuum Ultraviolet Spectroscopy*, (Pied Publications, Lincoln, Nebraska, 1967) p.2.
- [2] Y. Hatano, In: *Dynamics of Excited Molecules*, K. Kuchitsu (eds.), Elsevier, Amsterdam, 1994, p.186.
- [3] R. L. Platzman, *Radiat. Res.* **17** (1962) 419.
- [4] K. Mitsuke, H. Hattori, and Y. Hikosaka, *J. Electron Spectrosc. Relat. Phenom.* **112** (2000) 137.
- [5] H. Nakamura, *J. Phys. Chem.* **88** (1984) 4812.
- [6] H. W. Kroto, J. R. Heath, S. C. O'Brien, R. F. Curl, and R. E. Smalley, *Nature* **318** (1985) 162.
- [7] H. W. Kroto, *Science* **242** (1998) 1139.
- [8] W. Krätschmer, Lowell D. Lamb, K. Fostiropoulos, and D. R. Huffman, *Nature* **347** (1990) 354.
- [9] H. Shinohara, *Rep. Prog. Phys.* **63** (2000) 843.
- [10] R. C. Haddon *et al.*, *Nature* **350** (1991) 320.
- [11] K. Holczer, O. Klein, S-M. Huang, R. B. Kaner, K-J. Fu, R. L. Whetten, and F. Diederich, *Science* **252** (1991) 1154.
- [12] E. A. Katz, D. Faiman, S. M. Tuladhar, J. M. Kroon, M. M. Wienk, T. Fromherz, F. Padinger, C. J. Brabec, and N. S. Sariciftci, *J. Appl. Phys.* **90** (2001) 5344.
- [13] N. S. Sariciftci, L. Smilowitz, A. J. Heeger, and F. Wudl, *Science* **258** (1474) 1992).
- [14] C. J. Brabec, N. S. Sariciftci, and J. C. Humelen, *Adv. Funct. mater* **11** (2001) 15.

- [15] I. V. Hertel, H. Steger, J. de Vries, B. Weisser, C. Menzel, B. Kamke, and W. Kamke, *Phys. Rev. Lett.* **68** (1992) 784.
- [16] R. K. Yoo, B. Ruscic, and J. Berkowitz, *J. Chem. Phys.* **96** (1992) 911.
- [17] S. Aksela, E. Nömmiste, J. Jauhiainen, E. Kukk, J. Karvonen, H. G. Berry, S. L. Sorensen, and H. Aksela, *Phys. Rev. Lett.* **75** (1995) 2112.
- [18] J. Kou, T. Mori, M. Ono, Y. Haruyama, Y. Kubozono, and K. Mitsuke, *Chem. Phys. Lett.* **374** (2003) 1.
- [19] J. Kou, T. Mori, S. V. K. Kumar, Y. Haruyama, Y. Kubozono, and K. Mitsuke, *J. Chem. Phys.* **120** (2004) 6005.
- [20] A. Reinköster, S. Korica, G. Prümper, J. Viefhaus, K. Godehusen, O. Schwarzkopf, M. Mast, and U. Becker, *J. Phys. B, At. Mol. Opt. Phys.* **37** (2004) 2135.
- [21] P. N. Juranic, D. Lukic, K. Barger, and R. Wehlitz, *Phys. Rev. A* **73** (2006) 042701.
- [22] K. Mitsuke, H. Katayanagi, B. P. Kafle, C. Huang, H. Yagi, Md. S. I. Prodhan, and Y. Kubozono, *J. Phys. Chem. A* **111** (2007) 8336.
- [23] J. Kou, T. Mori, Y. Kubozono, and K. Mitsuke, *Phys. Chem. Chem. Phys.* **7** (2005). 119.
- [24] H. Gaber, R. Hiss, H. G. Busmann, and I. V. Hertel, *Z. Phys. D* **24** (1992) 307.
- [25] D. Muigg, G. Denifl, P. Scheier, K. Becker, and T. D. Märk, *J. Chem. Phys.* **108** (1998) 963.
- [26] S. W. J. Scully, E. D. Emmons, M. F. Gharaibeh, R. A. Phaneuf, A. L. D. Kilcoyne, A. S. Schlachter, S. Schippers and A. Müller, H. S. Chakraborty M. E. Madjet, and J. M Rost, *Phys. Rev. Lett.* **94** (2005) 065503-1.

- [27] P. Colavita, G. De Alti, G. Fronzoni, M. Stener, and P. Decleva, *Phys. Chem. Chem. Phys.* **3** (2001) 4481.
- [28] H. Yasumatsu, T. Kondow, H. Kitagawa, K. Tabayashi, and K. Shobatake, *J. Chem. Phys.* **104** (1996) 899.
- [29] R. Jaensch and W. Kamke, *Mol. Mater.* **13** (2000) 143.
- [30] W. Kamke, private communication, revised data of ref. 12.
- [31] T. Mori, J. Kou, Y. Haruyama, Y. Kubozono, and K. Mitsuke, *J. Electron Spectrosc. Relat. Phenom.* **144-147** (2005) 243.
- [32] J. Abrefah, D. R. Olander, M. Balooch, and W. J. Siekhaus, *Appl. Phys. Lett.* **60** (1992) 1313.
- [33] V. Piacente, G. Gigli, P. Scardala, A. Giustini, and D. Ferro, *J. Phys. Chem.* **99** (1995) 14052.
- [34] R. Jaensch, and W. Kamke, *Mol. Mater.* **13** (2000) 163.
- [35] C. K. Mathews, M. Sai Baba, T. S. L. Narasimhan, R. Balasubramanian, N. Sivaraman, T. G. Srinivasan, and P. R. V. Rao, *J. Phys. Chem.* **96** (1992) 3566.
- [36] S. H. Schwartz, A. Fardi, K. Haghghat, A. Langereis, H. T. Schmidt, and H. Cederquist, *Phys. Rev. A* **63** (2000) 013201.
- [37] J. R. Huber, *Pure and Appl. Chem.* **60** (1988) 947.
- [38] R. Bersohn, in: *Molecular Photodissociation Dynamics*, M. N. R. Ashfold, and J. E. Baggot (eds.), The Royal Society of Chemistry, London, 1987, Chap.1.
- [39] K. Mitsuke, H. Katayanagi, J. Kou, T. Mori, and Y. Kubozono, *Am. Inst. Phys. CP* **811** (2006) 161.
- [40] A. T. J. B. Eppink, D. H. Parker, *Rev. Sci. Instrum.* **68** (1997) 3477.
- [41] D. A. Dahl, SIMION 3D 7.0, Boise Idaho: Scientific Instrument Services Inc. 2000.

Chapter 2

2. Basic theory of photoabsorption by an atom or molecule

2.1 The absorption line

If linearly polarized light with a continuous spectrum is allowed to fall onto an absorption cell containing a low-pressure gas, the attenuation of light occurs. The attenuation profile may be represented as in Fig. 2.1, where the transmitted intensity I_ν (defined as the energy transmitted per second in unit solid angle and through unit area perpendicular to the beam per unit frequency interval) is a function of the frequency ν (spectrum centered on ν).

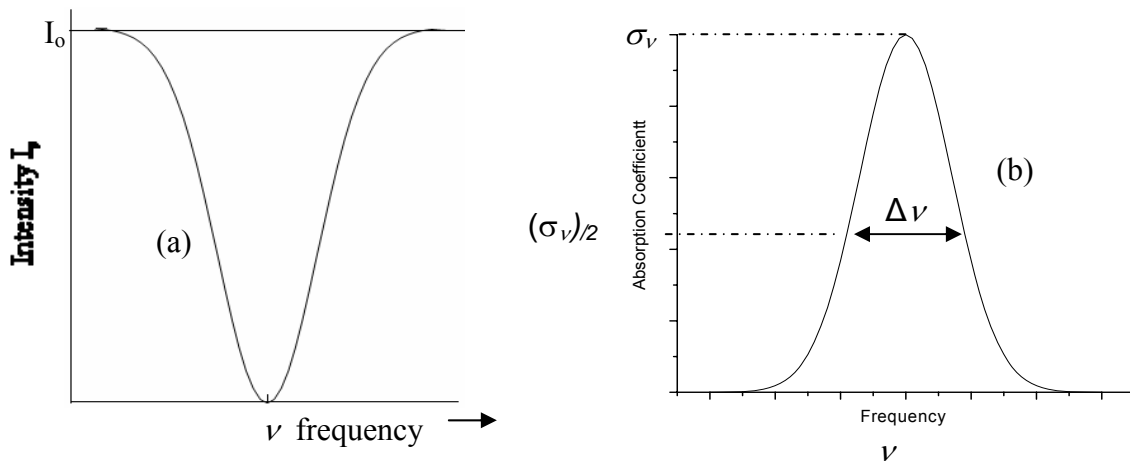


Fig 2.1 (a), the attenuation profile for an absorption line; (b), the absorption coefficient profile for an absorption line. Figures are taken from Ref. (1).

If an electromagnetic radiation having a bandwidth between w and $w + dw$, and intensity $I(w)$ (where $w = 2\pi\nu$) is permitted to pass through a gas cell of thickness dx , the radiation exiting from the cell will have been attenuated by $dI(w)$, which can be written as

$$dI(w) = \sigma_{os}(w)I(w)N_0dx . \quad (2.1)$$

Here N_0 is the number density of molecules of the gas in some lower (ground) state and the equation Eq. (2.1) serves to define an absorption cross section $\sigma_{os}(w)$ corresponding to a transition between the lower state 0 and upper state s . Application of Fig. 2.1(a) and Eq. (2.1) allows the variation of absorption cross section as a function of frequency to be obtained as in Fig. 2.1(b) [1].

The incident radiation induces transitions from the lower state 0 to a state s , thereby reducing the number density N_0 . This is described by the equation

$$-\frac{dN_0}{dt} = N_0 \int B_{os}(w) \rho(w) dw \quad (2.2)$$

where $\rho(w) = I(w)/c$ is the energy density of the electromagnetic radiation and $B_{os}(w)$ is the Einstein coefficient for induced absorption as given by the following equation;

$$B_{os}(w) = \frac{4\pi^2}{3h^2} \left| \langle s | e \sum_j x_j | 0 \rangle \right|^2. \quad (2.3)$$

Here, the quantity in bra-ket is the electric dipole matrix element.

2.2 Photoabsorption cross section and Oscillator strength

If an electron bound to a nuclear framework possessed perfect oscillating properties following harmonic motion, then according to classical theory the excitation probability of this electron would be said to have an *oscillator strength*, f_n , of one. The concept of the optical oscillator strength has been developed for providing a useful measure of the transition probability [2-4].

The notion of the oscillator strength is originally due to Thomson. Later Heisenberg and Kramers derived the same expression from quantum mechanics, as summarized by Fano and Cooper [5]. An explicit derivation on this parameter is given in the references [2,3] and also included (only relevant part) in the appendix 2 of this thesis. Berkowitz [2] and Inokuti [3] have explained nicely how the derivation on this parameter obtained from classical theory and that from the quantum mechanics

are related. In classical theory electrons are considered as bound to their equilibrium position by a restoring force proportional to their displacement $x(t)$ at time t , and thus undergoing harmonic oscillation at natural (angular) frequency ω_n . In the other hand, quantum mechanically one must consider the mean value of the displacement x (or equivalently, the mean value of the induced dipole moment ex) when an external field is imposed upon an atomic or molecular system). More importantly, Fano and Cooper [5] gave the prescription for evaluating f_s as

$$f_s = \left(\frac{2m\omega_s}{3\hbar} \right) \left| \langle s | \sum_j x_j | 0 \rangle \right|^2, \quad (2.4)$$

Here f_s is expressed in terms of the dipole matrix element squared $\left| \langle s | \sum_j x_j | 0 \rangle \right|^2$ between the ground state 0 and the excited states.

The above equation can also be expressed as

$$f_s = \left(\frac{8\pi^2 m_e \nu}{3h} \right) \mu^2. \quad (2.5)$$

Where μ is the induced transition dipole moment or dipole strength corresponding to the electronic transition.

Moreover, the oscillator strength distribution df/dE is proportional to absolute photoabsorption cross section $\sigma_{\text{abs,A}}$ at the photon energy E :

$$\sigma_{\text{abs,A}} = \frac{e^2 h}{4 \epsilon_0 m_e c} \frac{df}{dE} = 1.098 \times 10^{-20} \frac{df}{dE}. \quad (2.6)$$

Here, $\sigma_{\text{abs,A}}$ is in m^2 and E is in eV. For calculations values of parameters used are as follows: the electron charge e of 1.602×10^{-19} C, the Planck constant h of 6.626×10^{-34} J s, the vacuum permittivity ϵ_0 of 8.854×10^{-12} $\text{C}^2 \text{J}^{-1} \text{m}^{-1}$, the electron rest mass m_e of

9.109×10^{-31} kg, the velocity of light c of 2.998×10^8 m s⁻¹. Integration of eq. (2.6) leads to the oscillator strength f in the $h\nu$ range from E_1 to E_2 as

$$f = \int_{E_1}^{E_2} \frac{df}{dE} dE = \int_{E_1}^{E_2} \frac{\sigma_{\text{abs,A}}}{1.098 \times 10^{-20}} dE \quad (2.7)$$

The total oscillator strength f_{total} including discrete and continuum spectra should agree with the total number N of electrons in the molecule:

$$f = \int_{E_0}^{\infty} \frac{df}{dE} dE = \int_{E_0}^{\infty} \frac{\sigma_{\text{abs,A}}}{1.098 \times 10^{-20}} dE = N \quad (2.8)$$

Here E_0 indicates the transition energy from the initial vibronic ground state to the vibrational ground level of the lowest electronically excited state. This relation is called the Thomas-Kuhn-Reiche (TKR) sum rule.

References

- [1] G. V. Marr, In: *Photoionization Processes in Gases*, Academic Press, New York (1967) p. 6.
- [2] J. Berkowitz, In: *Photoabsorption, Photoionization, and Photoelectron Spectroscopy*, Academic Press, New York (1979) p. 59.
- [3] M. Inokuti, *Photochem. Photobiol.* **44** (1986) 279.
- [4] Y. Hatano and M. Inokuti, In: M. Inokuti (ed.), *Atomic and Molecular Data for Radiotherapy and Radiation Research*, IAEA, Vienna (1995) Chap. 5.
- [5] U. Fano and J. W. Cooper, *Rev. Mod. Phys.* 40 (1968) 441.

Chapter 3

3 Experiment

3.1 Overview

In this chapter, description is made on the experimental arrangements used for the quantitative studies of photoionization cross sections of C_{60} .

All the experiments have been carried out using a monochromatized synchrotron from the 18 m spherical grating monochromator connected to the bending magnet beamline 2B of the UVSOR synchrotron radiation facility at the Institute for Molecular Science. The experimental setup mainly consists of an 18 m spherical grating Dragon type monochromator [1-2], a time-of-flight (TOF) mass spectrometer, a water cooled thickness monitor, a photodiode (or a gold mesh), and a heat reflector into which sample holder (situated at 45.3 mm below from the ionization region) is kept. Typical arrangements of the apparatus (TOF spectrometer and other electronic devices) are shown in Fig. (3.2). The mass spectrometer, which has been kept inside the experimental chamber (Fig. 3.3), was arranged in such a way that center of the ion repeller and extracting electrodes coincide with the focal point of the post focusing mirror of the beamline. A supersonic molecular beam flowing through a hole at the top of the heat reflector was collided with a photon beam in the photoionization region. The photoions thus produced are extracted by the acceleration field, traveled in the drift tube, and detected by a microchannel plate (MCP) in order to measure the mass spectra or photoionization yield curves. This experimental setup is basically the same with that of employed originally by Mori *et al.* [3] and Mitsuke *et al.* [4] for the study optical properties of fullerene family.

3.2 Synchrotron Radiation and Monochromator

Ultraviolet Synchrotron Orbital Radiation (UVSOR) facility in IMS consists of a 15 MeV linear accelerator (liniac) as an electron beam pre-injector, a booster electron synchrotron (about 8.5 m diameter) for accelerating the electron beam up to 750 MeV, and a 750 MeV electron storage ring for producing synchrotron radiation [5]. The electron beam injected from the liniac and accelerated by the synchrotron accelerator is further injected into the storage ring, and accelerated up to 750 MeV. The storage ring has a quasi-octagonal shape with the combination of 8 bending magnets and 8 straight sections. In straight sections, four undulators are installed for producing higher brightness synchrotron radiation. Furthermore, a radio-frequency RF cavity is used to compensate the energy of the electron beam lost by emitting synchrotron radiation. When UVSOR is operated in its multi bunch mode, the electrons are stored with into 16 bunches. Main parameters of the UVSOR accelerator complex are summarized in Table 3-1.

Table 3-1

General parameters of the storage ring

Circumference	53.2 m
Energy	750 MeV (600 MeV at injection)
Number of bunches	Multi-bunch Mode: 16 Single bunch Mode:1
Initial stored current	Multi-bunch mode: 300 mA (max.500 mA) Single bunch Mode: 60-70 mA(max.100 mA)
Beam lifetime	Multi-bunch Mode: 8h (at 200 mA) Single bunch Mode: 1h (50 mA)

Beam sizes	0.39 mm (horizontal) 0.27 mm (vertical)
Pulsed light period	Multi-bunch Mode: 11 ns Single bunch Mode: 176 ns
Pulsed light width	~ 1 ns (min. 20 ps) with a harmonic cavity system
Vacuum pressure	$\sim 1 \times 10^{-10}$ Torr

The Beamline BL2B in UVSOR has been utilized for the study of photoionization and reaction dynamics of various fullerenes in gas phase ([4] and reference therein). As shown in the schematic diagram of this beam line (side view) in the Fig (3.1), synchrotron radiation emitted from the storage ring is focused onto the entrance slit by two pre-focusing mirrors. The incident SR was monochromatized by the Dragon type monochromator which covers the $h\nu$ range from 25 to 150 eV with three gratings: G1 for 80 - 150 eV; G2 for 40 - 100 eV and G3 for 25 - 50 eV [1]. After passing through the movable exit slit, the monochromatized light is refocused into the photoionization region by the post-focusing mirror (toroidal type). When the entrance- and exit- slit widths were set to 300 μm , the resolution (the full width at half maximum) which was determined by the measurement of the photon energy was estimated to be 8.5 meV of the members of the $3s^{-1}np$ Rydberg series of argon which lie at $h\nu = 25\text{-}30$ eV [2]. The details of the monochromator have been published elsewhere [1,2]. Output spectrum (photon flux versus energy) of this monochromator measured during this experiment is shown in Fig. 3.4. The wavelength scan is performed by the stepping motor controlled on the CAMAC dataway by a personal computer.

The first-order light monochromatized by the grating G2 was subject to contamination of the second-order light. The $h\nu$ dependence of the percentage of the second-order light was estimated by measuring the ion yield spectrum of He at $h\nu = 40 - 100$ eV [4] (contamination of the third and fourth order lights were considered to be negligible and were not evaluated). The percentage was determined as an adjustable parameter to reproduce the observed spectrum from the absorption cross section data of He [6]. For instance, the percentage at $h\nu = 40$ eV was found to be 22 %. Alternatively, the percentage of the second-order light could be calculated based on the Kr^+ yield spectra of Kr in the vicinity of the $3d_{5/2}^{-1} 5p^1$ resonance peaks appearing at 45.6 and 91.2 eV, with the aid of the reported partial photoionization cross sections [7] of Kr at around 45 and nearly 90 eV. The resultant percentage was 23% at ~ 45 eV, which accords well with the value obtained using the ion yield spectrum of He.

3.3 Experimental chamber and vacuum system

The experimental chamber is evacuated by a turbomolecular pump with (respective to) its pumping speed of 1000 l/s. The typical background pressure is 1.1×10^{-8} Torr without a sample gas. Moreover, a differentially pumping chamber has been set between the experimental chamber and the post-focusing mirror which is pumped by an ion pump and supported by two turbo molecular pumps of pumping speed of 340 l/s installed near the both ends of this chamber. When the sample gas is introduced, the background pressure of up to $\sim 1 \times 10^{-5}$ Torr is allowed in the experimental chamber with keeping the pressure in the post-focusing mirror chamber $\sim 1.5 \times 10^{-9}$ Torr. Typically, during the experiments the pressure of the chamber was kept to be $\sim 1 \times 10^{-6}$ to 2×10^{-7} Torr.

To shield the photoionization region from the external magnetic field, the μ -metal shield is equipped inside the experimental chamber.

3.4 Experimental procedure and data acquisition system

Figure (3.2) shows the side view of the apparatus. The spectrometer is of the Wiley-McLaren type [8] double focusing time of flight (TOF) mass spectrometer. It consists of first and second acceleration regions, a 348 mm drift tube, and dual microchannel plates. The powder of the C_{60} with purity of 99.98% loaded in a quartz tube and further purified by eliminating the organic solvent such as benzene or toluene through heating the samples for 1 day (12 h) in a vacuum at nearly 200°C. In order to produce a molecular beam of C_{60} , sample holder was heated up to 703 to 773 K with a resistive heater. An exit hole of the quartz tube was 1 or 2.5 mm in diameter. The molecular beam was then collimated by an orifice of 4.6 mm in diameter drilled on a heat reflector.

Monochromatized synchrotron radiation was focused onto the molecular beam and photoions were produced in the intersection region. A pulsed voltage rising from the ground level to +80 V (duration = 4.5 μ s, frequency = 10 kHz) was applied to the ion repeller electrode as a start trigger for the TOF measurement. The photoions extracted by this pulsed electric field were mass separated by a double-focusing time-of-flight (TOF) mass spectrometer, and detected with a secondary electron multiplier comprised of two microchannel plates (MCPs) having an effective diameter of 27 mm (Hamamatsu, F1552). The entrance surface of the front MCP was biased to the voltage of -2.1 kV, while the exit surface of the back MCP was grounded. The signal from MCP was fed into a time to digital converter and then processed by conventional pulse counting system. Ion signal counts were obtained by the integration over the respective mass peaks. Simultaneously the fluxes of synchrotron radiation and

molecular beam were measured throughout an experimental run using a silicon photodiode and crystal-oscillator surface thickness monitor, respectively. A photoion yield spectrum was obtained by normalizing the integrated ion counts at each $h\nu$ for the photon and molecular-beam fluxes, and by collecting the normalized counts consecutively with changing $h\nu$.

References

1. M. Ono, H. Yoshida, H. Hattori, and K. Mitsuke, Nucl. Instrum. Methods Phys. Res. A **467** (2001) 577.
- [2] H. Yoshida and K. Mitsuke, J. Synchrotron Rad. **5** (1998) 774.
- [3] T. Mori, J. Kou, M. Ono, Y. Haruyama, Y. Kubozono, and K. Mitsuke, Rev. Sci. Instrum. **74** (2003) 3769.
- [4] K. Mitsuke, H. Katayanagi, B. P. Kafle, C. Huang, H. Yagi, Md. S. I. Prodhon, and Y. Kubozono, J. Phys. Chem. A **111** (2007) 8336.
- [5] UVSOR Pumplet (2006), Pg. 3.
- [6] J. M. Bijau and F. J. Wuilleumier, J. Electron Spectrosc. Relat. Phenom. **71** (1995) 205.
- [7] N. Saito and H. I. Suzuki, Int. J. Mass Spec. Ion Proc. **115** (1992) 157.
- [8] W. C. Wiley and I. H. McLaren, Rev. Sci. Instrum. **26** (1955) 1150.

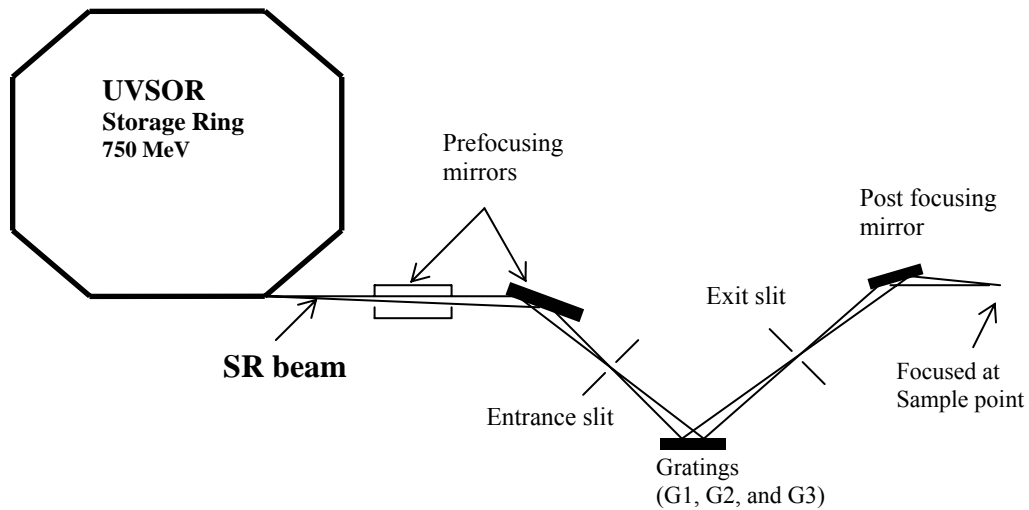


Fig. 3.1. Schematic diagram (side view) of BL2B equipped with an 18 m spherical grating monochromator, entrance and exit slits, and pre-focusing and post focusing mirrors [2].

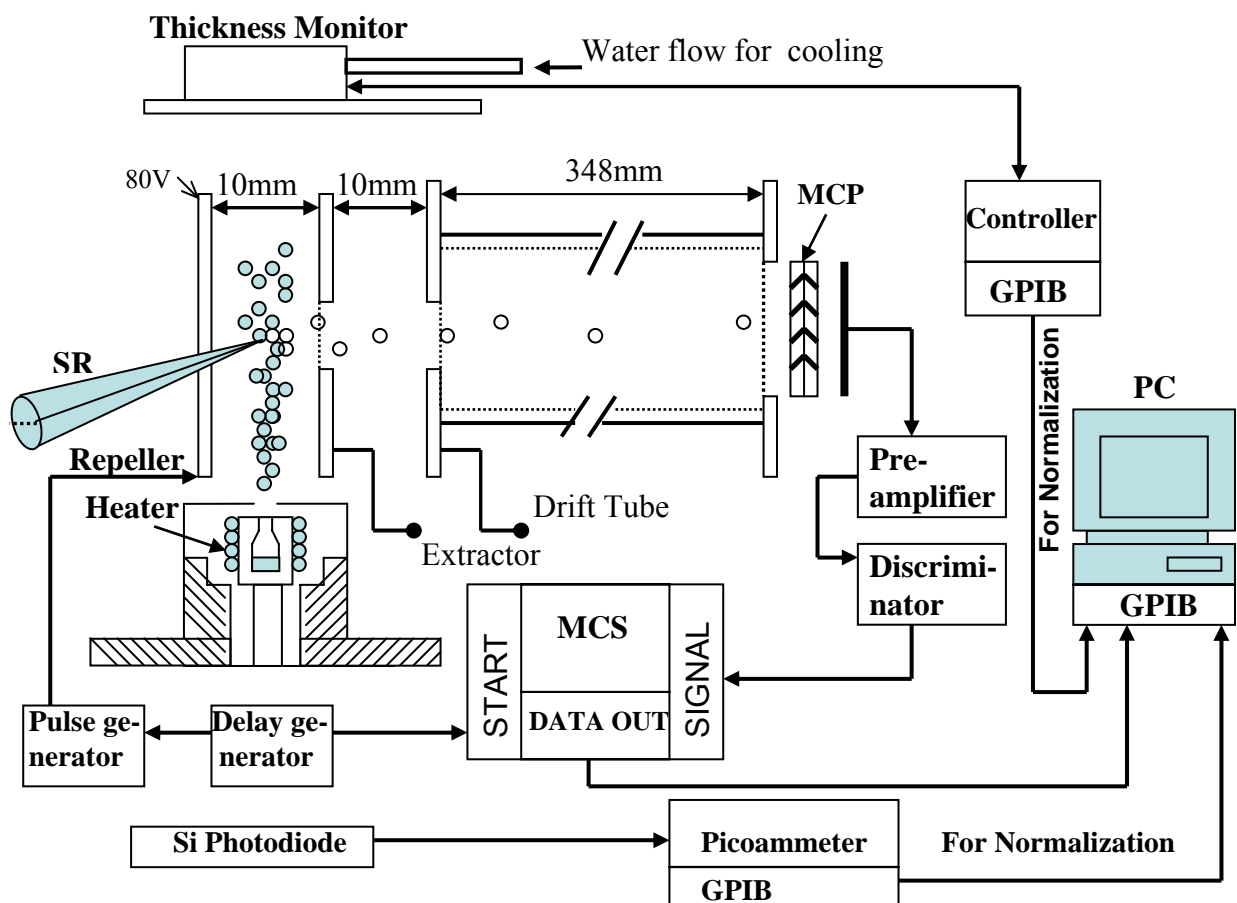


Fig. 3.2. Schematic diagram of apparatus for the photoionization spectrometer and data acquisition system. SR, monochromatized synchrotron radiation; MCS, multichannel scaler; MCP, microchannel plate electron multiplier; PC, personal computer. This figure was reproduced from Ref. (4).

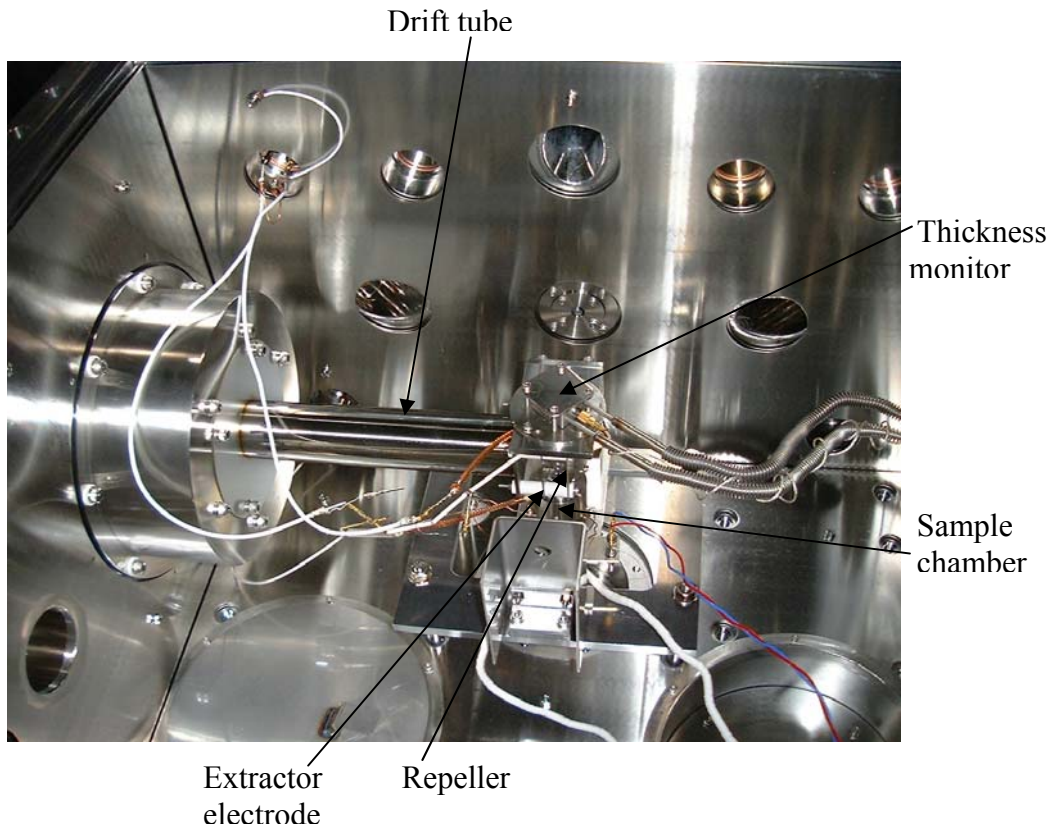


Fig. 3.3. A photograph of the photoionization spectrometer (the double focusing TOF spectrometer) assembled inside the experimental chamber in BL2B.

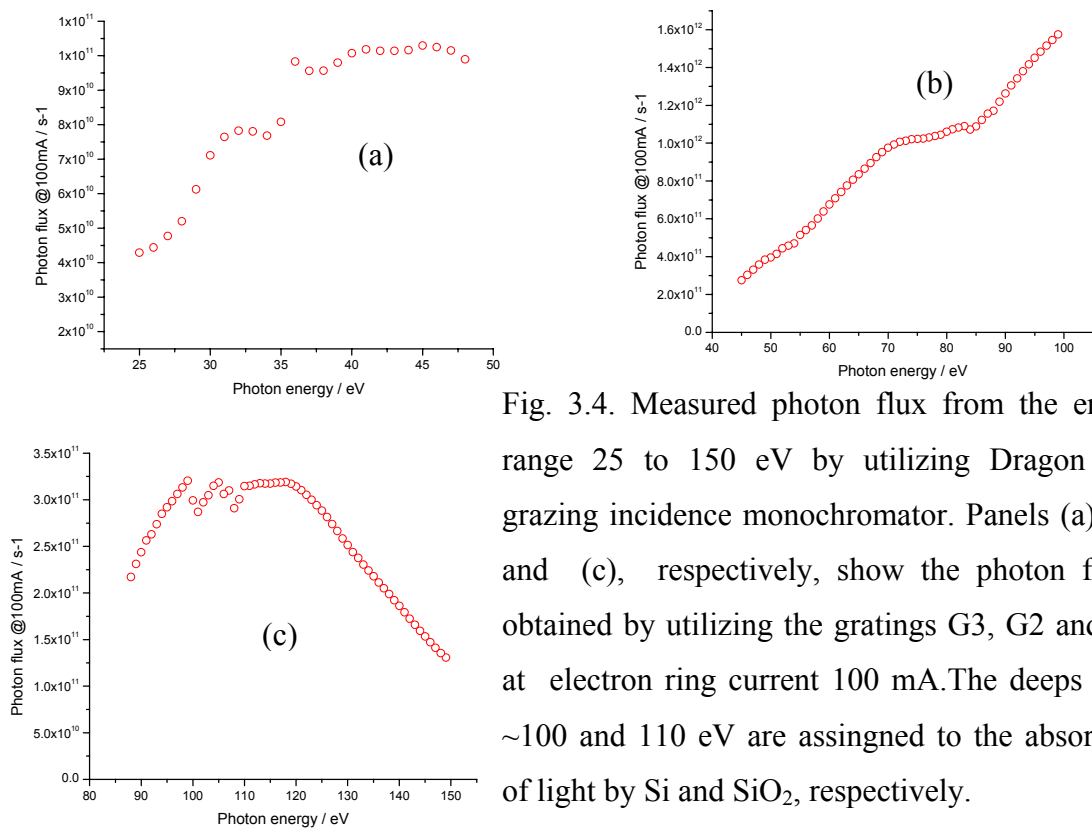


Fig. 3.4. Measured photon flux from the energy range 25 to 150 eV by utilizing Dragon type grazing incidence monochromator. Panels (a), (b), and (c), respectively, show the photon fluxes obtained by utilizing the gratings G3, G2 and G1, at electron ring current 100 mA. The deeps at $h\nu \sim 100$ and 110 eV are assigned to the absorption of light by Si and SiO₂, respectively.

Chapter 4

4. Absolute Total Photoionization Cross Section of C₆₀ in the Range of 25 - 120 eV

[J. Phys. Soc. Jpn **77** (2008) 014302-1-5]

4.1. Introduction:

The interaction of C₆₀ with high-energy photons has attracted considerable attention, since C₆₀ provides a unique molecular system characterized by an exceptionally stable electronic structure associated with dense and highly degenerated molecular orbitals and by extremely large vibrational degrees of freedom. Many groups have measured the relative photoionization cross section of C₆₀⁺ from C₆₀ by means of mass spectrometry in the extreme UV region [1-8]. Some authors have reported [1,4-9] that this cross section curve shows peaks and shoulders at photon energies below $h\nu \sim 50$ eV, reflecting the molecular character of C₆₀ in its valence photoionization. In contrast, the yield curve above ~ 50 eV appears to resemble the absorption cross section of an isolated carbon atom.

In 2004, Kou *et al.* [5] measured relative partial cross sections for production of singly and doubly charged ions from C₆₀ at $h\nu = 25 - 150$ eV. From the sum of the two partial cross sections, they derived a relative total photoionization cross section of C₆₀. This total cross section may accord with the photoabsorption cross section of C₆₀, since the photoionization quantum yield is considered to be nearly equal to unity in this $h\nu$ region [5,10] and the contribution of triply or highly charged C₆₀^{z+} is much smaller. Nevertheless, the total cross section proposed by Kou *et al.* [5] was not proportional to the theoretical absolute photoabsorption cross section of C₆₀ obtained by Colavita *et al.* [9]. Very recently, we have [8] investigated the dependence of the

detection efficiency of the ion detector on the mass-to-charge ratio (m/z) and concluded that the relative partial cross section for double photoionization of C_{60} should be about one third as large as Kou *et al.* had expected. In this connection Reinköster *et al.* [6] and Juranic *et al.* [7] have reported that the sum of the relative partial cross sections for C_{60}^{z+} ($z = 1-3$) from C_{60} is consistent with the photoabsorption cross section by Colavita *et al.* [9].

To obtain an absolute photoionization or photoabsorption cross section curve of C_{60} is another important issue that still remains to be settled. Generally speaking, if the sample is nonvolatile and its vapor pressure data is unreliable, one should be confronted with many difficulties in accurately estimating the absolute number density and effective path length of the interaction region in a windowless sample gas chamber. Actually there exist only a few experimental works on the measurements of absolute total photoionization cross section $\sigma_{\text{abs,I}}$ and absolute photoabsorption cross section $\sigma_{\text{abs,A}}$ of C_{60} in the extreme UV region [2,11-14]. In 1999, Berkowitz examined a $\sigma_{\text{abs,A}}$ spectrum of C_{60} in the energy range of 3 - 340 eV by compiling the experimental cross section data then available [10]. In 2000, Jaensch and Kamke [12,13] determined the $\sigma_{\text{abs,A}}$ curve at the photon energy range from 10 to 26 eV by a photon attenuation method, using a gas chamber filled with C_{60} vapor and applying the Lambert-Beer law (gas chamber technique). Their cross section data were significantly lower than those compiled by Berkowitz [10] at $h\nu = 10 - 26$ eV. For instance, the cross section value at $h\nu = 24.5$ eV by Berkowitz was 1100 - 1200 Mb and that by Jaensch and Kamke was approximately 650 Mb. In 2004, Mori *et al.* carried out mass spectrometric study of C_{60} using synchrotron radiation and obtained a $\sigma_{\text{abs,I}}$ curve ($\sim\sigma_{\text{abs,A}}$) at $h\nu = 24.5 - 150$ eV from the ion yields [14]. Their cross

section value was 762 Mb at $h\nu = 24.5$ eV, which lies between the cross sections reported by the former two papers.

The analysis conducted by Mori *et al.* [14] was based essentially on the data of Kou *et al.* [5], i.e., the partial cross sections for the production of singly and doubly charged ions from C_{60} . Kou *et al.*, however, neglected both the m/z -dependence of the detection efficiency η and the contribution of triply charged ions. It is therefore likely that $\sigma_{\text{abs,I}}$ of Mori *et al.* in a higher $h\nu$ region deviates from the proper total photoionization cross section. In the present paper, we will reevaluate $\sigma_{\text{abs,I}}$ from $h\nu = 25$ to 120 eV by taking account of η of the ion detector. Introducing a plausible functional form of η may bring about an appreciable modification of the relative partial cross sections for the doubly and triply charged ions. Eventually, $\sigma_{\text{abs,I}}$ curve of C_{60} should be substantially modified. I will also present the oscillator strength distribution curve over a wide energy rang from 3.5 to 119 eV by combining the present $\sigma_{\text{abs,I}}$ and previously published $\sigma_{\text{abs,A}}$ curves.

4.2. Methodology

The experimental setup for photoionization mass spectrometry of the fullerenes which was employed in this experimental work has been described briefly in the chapter three of this thesis and described in detail in the Ref. (15).

In order to estimate the absolute partial cross section $\sigma_{\text{abs}}(z^+)$ for the formation of the ions in a charge state z from C_{60} the following expression has been utilized:

$$\sigma_{\text{abs}}(z^+) = \frac{R(z^+)}{\Phi n L F \tau} \cdot \frac{1}{\eta_{\text{abs}}(C_{60}^{z^+})} \quad (1a)$$

$$= \frac{2R(z^+) A S_2 k_B T}{\pi \Phi L l F D S_1} \cdot \frac{1}{\eta_{\text{abs}}(C_{60}^{z^+})} \quad (1b)$$

Here, $R(z^+)$ is the signal count rate of the photoions in a charge state z , Φ is the photon flux of synchrotron radiation, n is the number density of C_{60} in the ionization region, $L = 10$ mm is the length of the ionization volume along the light path, F is the repetition rate of the pulsed electric field, τ is the average residence time of the ions in the ionization volume under the field free condition, $\eta_{abs}(C_{60}^{z+})$ is the absolute overall detection efficiency of the apparatus for C_{60}^{z+} , A is the effective area of the thickness monitor, S_l and S_2 are the circular cross sections of the molecular beam at the thickness monitor and the light path (shown in Fig. 4.1), respectively, k_B is the Boltzmann constant, T is the absolute temperature of the sample holder (quartz tube), l is the length of ionization volume along the molecular beam path, and D is the mass deposition rate of the thickness monitor. In eq. (1a) the physical quantity having the largest uncertainty is the number density n of the C_{60} vapor in the ionization volume. We derived eq. (1b) on the presumption that the molecular beam is expanded conically from the circular hole of the heat reflector in an effusive-flow condition [12,14,20,21] with a diverging angle θ (see Fig.4.1). Detailed derivation of eq. (1b) from eq. (1a) is given in appendix 1.

In the earlier work by our group [14], the detection efficiency of the ions was assumed to be constant and substituted that of Kr ions for $\eta_{abs}(C_{60}^+)$ and $\eta_{abs}(C_{60}^{2+})$ in order to evaluate $\sigma_{abs}(z^+)$. However, recently, it was recognized that corrections for the m/z - dependence of the detection efficiency are critical to obtain accurate cross sections for photoionization of fullerenes [8]. In the present study, an evaluation of $\eta_{abs}(C_{60}^{z+})$ was made with the help of an empirical formula proposed by Twerenbold *et al.* [8,22] of the form

$$\eta = 1 - \exp\left[-\left(\frac{v}{53}\right)^{3.5}\right]. \quad (2)$$

Here, v denotes the velocity (in units of kms^{-1}), of the ion impinging on the entrance surface of the MCP assembly.

To inspect the applicability of the formula to our setup in the present study, first, the absolute overall detection efficiencies $\eta_{abs}(\text{Rg}^{z+})$ are experimentally determined of our mass spectrometer for singly and doubly charged photoions produced from three rare gases ($\text{Rg} = \text{Ar}, \text{Kr}, \text{Xe}$) as

$$\eta_{abs}(\text{Rg}^{z+}) = \frac{\sqrt{2}(k_B T)^{3/2}}{\sqrt{\pi} m_{\text{Rg}} P_{\text{Rg}}} \cdot \frac{R(\text{Rg}, z+)}{\Phi L' l F} \cdot \frac{1}{\sigma_{abs}(\text{Rg}^{z+})}. \quad (3)$$

Second, a functional form of η_{abs} from the least-squares fitting of the data points of $\eta_{abs}(\text{Rg}^{z+})$ is determined to the proposed formula (eq. 2). Here, $R(\text{Rg}^{z+})$ is the signal count rate of Rg^{z+} produced from Rg , m_{Rg} is the mass of a rare gas atom, and P_{Rg} is the sample pressure in the ionization region. The length of the ionization volume L' along the light path differs from L for C_{60} in eq. (1b). The partial cross sections $\sigma_{abs}(\text{Rg}^{z+})$ for the formation of singly and doubly charged rare gas ions are taken from the literature [23]. The $\eta_{abs}(\text{C}_{60}^{z+})$ values for C_{60}^{+} , C_{60}^{2+} , and C_{60}^{3+} are calculated using the formula of Twerenbold *et al.* and summarized in Table I. The overall detection efficiency is crucially dependent on m/z , since the ion acceleration voltage of 2.1 kV is not sufficient for a saturated operation of the MCP assembly. We used the $\eta_{abs}(\text{C}_{60}^{z+})$ values in Table I to evaluate the absolute partial cross sections from eq. (1b) for the formation of the ions in a charge state z from C_{60} .

4.3. Results and Discussion

4.3.1 Photoionization cross section

The absolute partial cross sections $\sigma_{abs}(+)$, $\sigma_{abs}(2+)$, and $\sigma_{abs}(3+)$ calculated from eq. (1b) are represented, respectively, by circles, triangles, and squares in Fig. 4.2. It is widely known that the $\sigma_{abs}(+)$ curve starts to rise at ~ 8 eV, reaches a broad

maximum at $h\nu \sim 20$ eV [1], and thereafter tends to decrease with increasing $h\nu$. Moreover, the curve displays several fine structures such as the two peaks at 26 and 34 eV and the flat area ranging 40–50 eV. These structures originate from ionization via the shape resonances as single electron excitation to vacant orbitals [4]. (It is worthwhile to clarify that we have observed these features (fine peaks at $h\nu = 26$ and 34 eV) repeatedly even after normalizing our photoion counts to the photon flux measured by using gold mesh. Thus these structures are not artifact as claimed by Scully *et al.* [24].) The $\sigma_{\text{abs}}(2+)$ curve shows a broad maximum of 24.8 Mb at $h\nu \sim 50$ eV above which it monotonically decreases. In contrast, $\sigma_{\text{abs}}(3+)$ has an onset at around 40 eV and steadily increases with $h\nu$. Each partial cross section includes the contribution of not only the parent but also fragment ions produced by the sequential loss of a C_2 unit. Hence, it is equal to the cross section involving all the ionic species in a particular charge state. The solid and dotted curves in Fig. 4.2 show the relative partial cross sections for the formation of singly and doubly charged ions, respectively, reported by Kou *et al.* [5]. The former curve is normalized to $\sigma_{\text{abs}}(+)$ at $h\nu = 80$ eV. At all photon energies, the dotted curve is noticeably higher than $\sigma_{\text{abs}}(2+)$, because Kou *et al.* disregarded the m/z dependence of the overall detection efficiency of the apparatus.

In Fig. 4.3, open circles represent the sum of $\sigma_{\text{abs}}(+)$, $\sigma_{\text{abs}}(2+)$, and $\sigma_{\text{abs}}(3+)$ which is nearly equal to $\sigma_{\text{abs,I}}$. Figure 4.3 also contains the $\sigma_{\text{abs,I}}$ and $\sigma_{\text{abs,A}}$ curves reported by Reinköster *et al.* [6] and Colavita *et al.* [9], respectively. The dashed curve by Reinköster *et al.* was normalized to $\sigma_{\text{abs,I}}$ by Yoo *et al.* at 40.8 eV [2], while the dotted curve by Colavita *et al.* is based on the theoretically determined absolute cross section. The present curve of $\sigma_{\text{abs,I}} = \sigma_{\text{abs}}(+) + \sigma_{\text{abs}}(2+) + \sigma_{\text{abs}}(3+)$ is in fair agreement with the dashed and dotted curves in the $h\nu$ range from ~ 45 to 120 eV. This may

prove the validity of our data analysis. Although the dashed curve of Reinkoster *et al.* deviates upward with decreasing $h\nu$ below 45 eV, some of its fine structures are reproduced in the present curve: shoulders at ~ 26 and ~ 40 eV are seen in both the curves [6,8]. The present $\sigma_{\text{abs,I}}$ data agree reasonably well at $h\nu > 50$ eV with 60 times the total photoabsorption cross section of a carbon atom [25] ($60 \times \sigma(\text{C})$) shown by squares in Fig. 4.3. This agreement indicates that at $h\nu > 50$ eV, photoabsorption of C_{60} is dominated by ionization of electrons in deeper molecular orbitals with larger binding energies [4].

In the present study, $\sigma_{\text{abs,I}}$ takes 401 Mb at $h\nu = 25.5$ eV. This value is a little smaller than $\sigma_{\text{abs,A}}$ determined by Jaensch and Kamke using the gas chamber technique [12 and 13] (~ 650 Mb at 24.5 eV and ~ 450 Mb at 25.5 eV) and $\sigma_{\text{abs,I}}$ obtained by Mori *et al.* [14] (762 Mb at $h\nu = 24.5$ eV). Detailed discussions on the accuracy of the present data and those of Jaensch and Kamke [12, 13] will be made in the next subsection, on the basis of analysis of the photoabsorption oscillator strength.

4.3.2 Photoabsorption oscillator strength

Single photon absorption excites a molecule from its initial ground state to a final electronically excited or ionized state. The concept of the optical oscillator strength has been developed for providing a useful measure of the transition probability [26-28]. The oscillator strength distribution df/dE is proportional to $\sigma_{\text{abs,A}}$ at the photon energy E :

$$\sigma_{\text{abs,A}} = \frac{e^2 h}{4 \varepsilon_0 m_e c} \frac{df}{dE} = 1.098 \times 10^{-20} \frac{df}{dE} \quad (4)$$

Here, e denotes the electron charge, h the Planck constant, ε_0 the vacuum permittivity ($8.854 \times 10^{-12} \text{ C}^2 \text{J}^{-1} \text{m}^{-1}$), m_e ($9.109 \times 10^{-31} \text{ kg}$) the electron rest mass, and c the velocity

of light ($2.998 \times 10^8 \text{ m s}^{-1}$). It should be noted that $\sigma_{\text{abs,A}}$ is in m^2 and E is in eV. Integration of eq. (3) leads to the oscillator strength f in the $h\nu$ range from E_1 to E_2 as

$$f = \int_{E_1}^{E_2} \frac{df}{dE} dE = \int_{E_1}^{E_2} \frac{\sigma_{\text{abs,A}}}{1.098 \times 10^{-20}} dE \quad (5)$$

The total oscillator strength f_{total} including discrete and continuum spectra should agree with the total number N of electrons in the molecule:

$$f_{\text{total}} = \int_{E_0}^{\infty} \frac{df}{dE} dE = \int_{E_0}^{\infty} \frac{\sigma_{\text{abs,A}}}{1.098 \times 10^{-20}} dE = N. \quad (6)$$

Here, E_0 indicates the transition energy from the initial vibronic ground state to the vibrational ground level of the lowest electronically excited state. This relation is called the Thomas-Kuhn-Reiche (TKR) sum rule.

The solid curve of Fig. 4.4 shows df/dE calculated using eq. (4) in the $h\nu$ range from 3.5 to 119 eV. Adopted cross sections are (a) the present $\sigma_{\text{abs,I}}$ at $h\nu = 25 - 119$ eV (circles), (b) $\sigma_{\text{abs,A}}$ measured by Jaensch and Kamke [12,13] at $h\nu = 11.4 - 25$ eV (triangles), and (c) $\sigma_{\text{abs,A}}$ measured by Yasumatsu *et al.* [11] at $h\nu = 3.5 - 11.4$ eV (squares). Here, the $\sigma_{\text{abs,A}}$ data of Yasumatsu *et al.* were reevaluated using the vapor pressure proposed by Jaensch and Kamke (4.5 Pa at 850K) or by dividing the original data of Yasumatsu *et al.* by 6. The reevaluated values agree well with $\sigma_{\text{abs,A}}$ of Jaensch and Kamke in an overlapping $h\nu$ region. To estimate f for a certain $h\nu$ range from eq. (5), the df/dE curve of Fig. 4.4 was plotted as a function of the frequency, and then integrated $df/d\nu$ over the corresponding frequency range by the trapezoidal method. The resultant f values for the $h\nu$ ranges from 3.5 to 40.8 eV and from 3.5 to 119 eV were 120.4 and 156.0, respectively. They are significantly smaller than the corresponding oscillator strengths of 187.6 and 233.4, respectively, expected from the TKR sum rule and $60 \times \sigma(\text{C})$ [10,29,30]. The insufficiency of f computed from Fig.

4.4 is entirely predictable because the $\sigma_{\text{abs,A}}$ data points of Jaensch and Kamke [12,13] lie much below those compiled by Berkowitz [10], as mentioned in §1 (see also Fig. 3 in ref. 14).

Conceivably, overestimation of the vapor pressure of C_{60} by Jaensch and Kamke gives rise to the discrepancy between the oscillator strengths calculated from Fig. 4.4 and those from the TKR sum rule and $60 \times \sigma(\text{C})$. Since the fullerene is a nonvolatile substance, difficulties in precise measurements of the vapor pressure have been impediment to the photoabsorption studies of C_{60} for the gas chamber technique [26]. Jaensch and Kamke prepared their own set of vapor pressure data [31] by measuring the mass flux of the C_{60} beam effused from the orifice drilled through the wall of a temperature-controlled gas chamber. They have cautioned that, with a conventional sonic nozzle, C_{60} molecules in the beam suffer from collisions with each other because the beam condition changes from effusive to viscous flow with increasing temperature above $\sim 700\text{K}$ owing to very large $\text{C}_{60}\text{--}\text{C}_{60}$ scattering cross sections [32]. By devising the design of the orifice, Jaensch and Kamke supposed that they can preserve an effusive flow condition for the C_{60} beam even at $\sim 773\text{K}$. Nevertheless, the vapor pressures that they obtained were higher by a factor of ~ 1.5 to 6 than those reported by other workers [20,21,33,34].

Many authors [10,35,36] have argued that the most dependable equilibrium vapor pressures of C_{60} are those given by Piacente *et al.* in 1995 [21]. Piacente *et al.* have precisely estimated the vapor pressure in the sample temperature range from 730 to 990 K by using two independent methods: the torsion- and Knudsen-effusion methods. Smith [34] and Coheur *et al.* [35] have derived $\sigma_{\text{abs,A}}$ of C_{60} in the UV and visible regions from the vapor pressure data of Piacente *et al.* Moreover, Smith and Coheur *et al.* exhibited an excellent agreement between $\sigma_{\text{abs,A}}$ of the gaseous C_{60} and

that in the solution of *n*-hexane after applying the Chako correction depending on the refractive index.

Relying on the vapor pressure data of Piacente *et al.* [21], the following alterations was made in $\sigma_{\text{abs,A}}$ and $\sigma_{\text{abs,I}}$ of Fig. 4.4 and summarized the revised cross sections in Fig. 4.5. First, $\sigma_{\text{abs,A}}$ of Yasumatsu *et al.* [11] was reevaluated by using the vapor pressure at 850 K of Piacente *et al.* [21], or by dividing $\sigma_{\text{abs,A}}$ of ref. 11 by 4. Second, $\sigma_{\text{abs,A}}$ of Jaensch and Kamke [12,13] was reevaluated using the vapor pressure at ~ 773 K of Piacente *et al.* [21] or by multiplying $\sigma_{\text{abs,A}}$ of ref. 13 by 1.5. Finally, the $\sigma_{\text{abs,I}}$ curve of the present study was redrawn after normalizing our data point at 25.5 eV to $\sigma_{\text{abs,A}}$ of Jaensch and Kamke, or by multiplying all our $\sigma_{\text{abs,I}}$ data by 1.5. The oscillator strengths were computed from the cross section curve in Fig. 4.5 and achieved 178.5 and 230.5 for the $h\nu$ ranges from 3.5 to 40.8 eV and from 3.5 to 119 eV, respectively. These values agree well with the oscillator strength expected from the TKR sum rule and $60 \times \sigma(\text{C})$, namely 187.6 and 233.4, respectively [10,29,30]. Therefore, it is concluded that the absolute photoabsorption cross section curve in Fig. 5 is more plausible than that in Fig. 4.4.

In Fig. 4.3, the solid curve designates the revised $\sigma_{\text{abs,I}}$ of the present study, which is obtained by elevating our original $\sigma_{\text{abs,I}}$ (open circles) by a factor of 1.5. The solid curve appears to be in a good agreement with the $\sigma_{\text{abs,I}}$ curve of Reinköster *et al.* [6]. In particular, the deviation at $h\nu < 45$ eV from the dashed curve becomes less detectable in the revised $\sigma_{\text{abs,I}}$ from the present study.

4.4. Conclusion

The absolute partial cross sections for single, double and triple photoionization of C₆₀ were experimentally determined in the energy range from 25 to 120 eV using tunable synchrotron radiation. Close evaluation of the absolute detection efficiency of our TOF spectrometer, the percentage of the second-order light, and the vapor pressure of C₆₀ above 700K allowed us to achieve an absolute total photoionization cross section curve. The oscillator strength was calculated from the present cross section curve, along with the absolute photoabsorption cross section curves at $h\nu = 3.5 - 25$ eV in the literature [11-13]. The oscillator strength for the $h\nu$ range from 3.5 to 40.8 eV is 178.5 and agrees well with that expected from the TKR sum rule and 60 times the total photoabsorption cross section of a carbon atom, $60 \times \sigma(\text{C})$.

References

- [1] I. V. Hertel, H. Steger, J. de Vries, B. Weisser, C. Menzel, B. Kamke, and W. Kamke, *Phys. Rev. Lett.* **68** (1992) 784.
- [2] R. K. Yoo, B. Ruscic, and J. Berkowitz, *J. Chem. Phys.* **96** (1992) 911.
- [3] S. Aksela, E. Nömmiste, J. Jauhiainen, E. Kukkk, J. Karvonen, H. G. Berry, S. L. Sorensen, and H. Aksela, *Phys. Rev. Lett.* **75** (1995) 2112.
- [4] J. Kou, T. Mori, M. Ono, Y. Haruyama, Y. Kubozono, and K. Mitsuke, *Chem. Phys. Lett.* **374** (2003) 1.
- [5] J. Kou, T. Mori, S. V. K. Kumar, Y. Haruyama, Y. Kubozono, and K. Mitsuke, *J. Chem. Phys.* **120** (2004) 6005.
- [6] A. Reinköster, S. Korica, G. Prümper, J. Viehhaus, K. Godehusen, O. Schwarzkopf, M. Mast, and U. Becker, *J. Phys. B, At. Mol. Opt. Phys.* **37** (2004) 2135.
- [7] P. N. Juranic, D. Lukic, K. Barger, and R. Wehlitz, *J. Phys. Rev. A* **73** (2006) 042701.
- [8] K. Mitsuke, H. Katayanagi, B. P. Kafle, C. Huang, H. Yagi, Md. S. I. Prodhan, and Y. Kubozono, *J. Phys. Chem. A, J. Phys. Chem. A* **111** (2007) 8336.
- [9] P. Colavita, G. De Alti, G. Fronzoni, M. Stener, and P. Decleva, *Phys. Chem. Chem. Phys.* **3** (2001) 4481.
- [10] J. Berkowitz, *J. Chem. Phys.* **111** (1999) 1446.
- [11] H. Yasumatsu, T. Kondow, H. Kitagawa, K. Tabayashi, and K. Shobatake, *J. Chem. Phys.* **104** (1996) 899.
- [12] R. Jaensch and W. Kamke, *Mol. Mater.* **13** (2000) 143.
- [13] W. Kamke, private communication, revised data of ref. 12.

- [14] T. Mori, J. Kou, Y. Haruyama, Y. Kubozono, and K. Mitsuke, *J. Electron Spectrosc. Relat. Phenom.* **144-147** (2005) 243.
- [15] T. Mori, J. Kou, M. Ono, Y. Haruyama, Y. Kubozono, and K. Mitsuke, *Rev. Sci. Instrum.* **74** (2003) 3769.
- [16] M. Ono, H. Yoshida, H. Hattori, and K. Mitsuke, *Nucl. Instrum. Methods Phys. Res. A* **467-468** (2001) 577.
- [17] H. Yoshida and K. Mitsuke, *J. Synchrotron Rad.* **5** (1998) 774.
- [18] J. M. Bijau and F. J. Wuilleumier, *J. Electron Spectrosc. Relat. Phenom.* **71** (1995) 205.
- [19] N. Saito, and H. I. Sujuki, *Int. J. Mass Spec. Ion Proc.* **115** (1992) 157.
- [20] J. Abrefah, D. R. Olander, M. Balooch, and W. J. Siekhaus, *Appl. Phys. Lett.* **60** (1992) 1313.
- [21] V. Piacente, G. Gigli, P. Scardala, A. Giustini, and D. Ferro, *J. Phys. Chem.* **99** (1995) 14052.
- [22] D. Twerenbold, D. Gerber, D. Gritti, Y. Gonin, A. Netuschill, F. Rossel, D. Schenker, and J. L. Vuilleumier, *Proteomics* **1** (2001) 66.
- [23] D. M. P. Holland, K. Codling, J. B. West, and G. V. Marr, *J. Phys. B* **12** (1979) 2465.
- [24] S. W. J. Scully, E. D. Emmons, M. F. Gharaibeh, R. A. Phaneuf, A. L. D. Kilcoyne, A. S. Schlachter, S. Schippers and A. Müller, H. S. Chakraborty M. E. Madjet, and J. M Rost, *Phys. Rev. Lett.* **94** (2005) 065503-1.
- [25] B. L. Henke, E. M. Gullikson, and J. C. Davis, *At. Data Nucl. Data Tables* **54** (1993) 218.
- [26] M. Inokuti, *Photochem. Photobiol.* **44** (1986) 279.

[27] Y. Hatano and M. Inokuti, in *Atomic and Molecular Data for Radiotherapy and Radiation Research*, ed. M. Inokuti, (IAEA, Vienna, 1995) Chap. 5.

[28] J. Berkowitz, in *Photoabsorption, Photoionization, and Photoelectron Spectroscopy* (Academic, New York, 1979) p. 59.

[29] In ref, (10) f_{total} was initially estimated to be 413, which exceeds the value expected from the TKR sum rule by 53. Berkowitz attributed this difference to an overestimation of df/dE at 3.1 - 40.8 eV. He therefore uniformly reduced f by 22 % and obtained 187.6 for the above $h\nu$ range.

[30] We evaluated the oscillator strength of $f = 233.4$ at $h\nu = 3.1 - 119$ eV as follows. First, we subdivided the $h\nu$ region into two: 3.1 - 40.8 eV and 40.8 - 119 eV. For the 3.1 - 40.8 eV region, we adopted the reported f of 187.6 from the TKR sum rule, (10,27), while, for the 40.8 - 119 eV region, we calculated f from $60 \times \sigma(C)$ of Henke et al. (24) using eq. (4).

[31] R. Jaensch and W. Kamke, *Mol. Mater.* **13** (2000) 163.

[32] A. Ruiz, J. Bretón, and J. M. Gomez Llorente, *Chem. Phys. Lett.* **270** (1997) 121.

[33] C. K. Mathews, M. Sai Baba, T. S. L. Narasimhan, R. Balasubramanian, N. Sivaraman, T. G. Srinivasan, and P. R. V. Rao, *J. Phys. Chem.* **96** (1992) 3566.

[34] S. H. Schwartz, A. Fardi, K. Haghghat, A. Langereis, H. T. Schmidt, and H. Cederquist, *Phys. Rev. A* **63** (2000) 013201.

[35] A. L. Smith, *J. Phys. B, At. Mol. Opt. Phys.* **29** (1996) 4975.

[36] P. F. Coheur, M. Carleer, and R. Colin, *J. Phys. B, At. Mol. Opt. Phys.* **29** (1996) 4987.

Table I. Absolute detection efficiency $\eta_{abs}(C_{60}^{z+})$ of our mass spectrometer for C_{60}^{z+} ions estimated using the formula proposed by Twerenbold *et al.*[21], when the acceleration energy of the MCP assembly is set to 2.1 kV.

	C_{60}^+	C_{60}^{2+}	C_{60}^{3+}
η_{abs}	1.361×10^{-3}	4.274×10^{-3}	7.878×10^{-3}

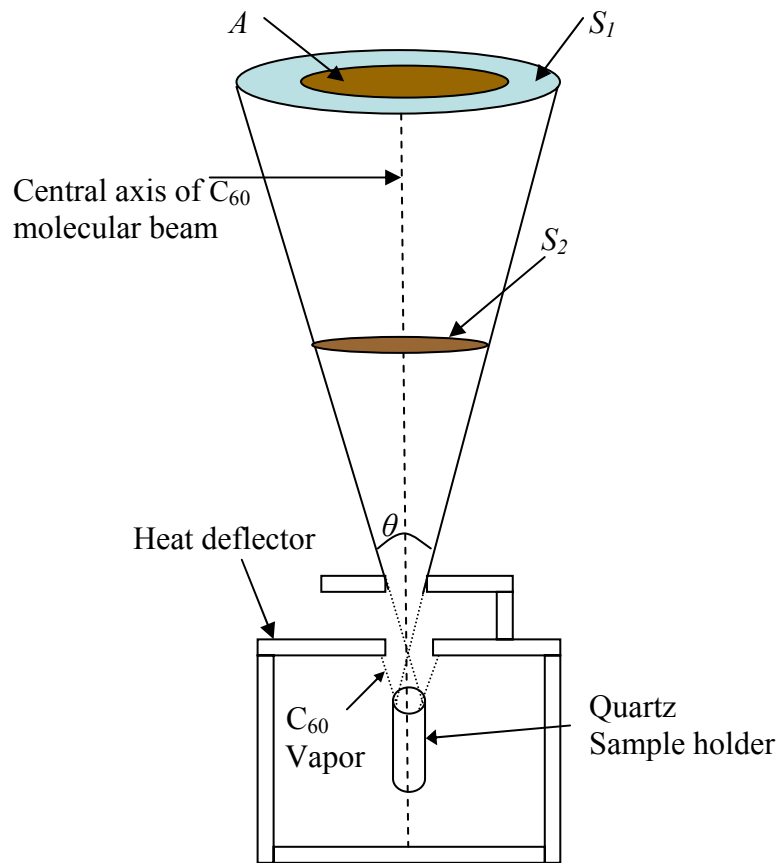


Fig. 4.1. Schematic diagram illustrating the effusion of the C_{60} molecular beam. A , effective area of the thickness monitor; S_1 , circular cross section of the molecular beam on the plane including the thickness monitor; S_2 , circular cross section of the molecular beam on the plane including the central axis of the light path.

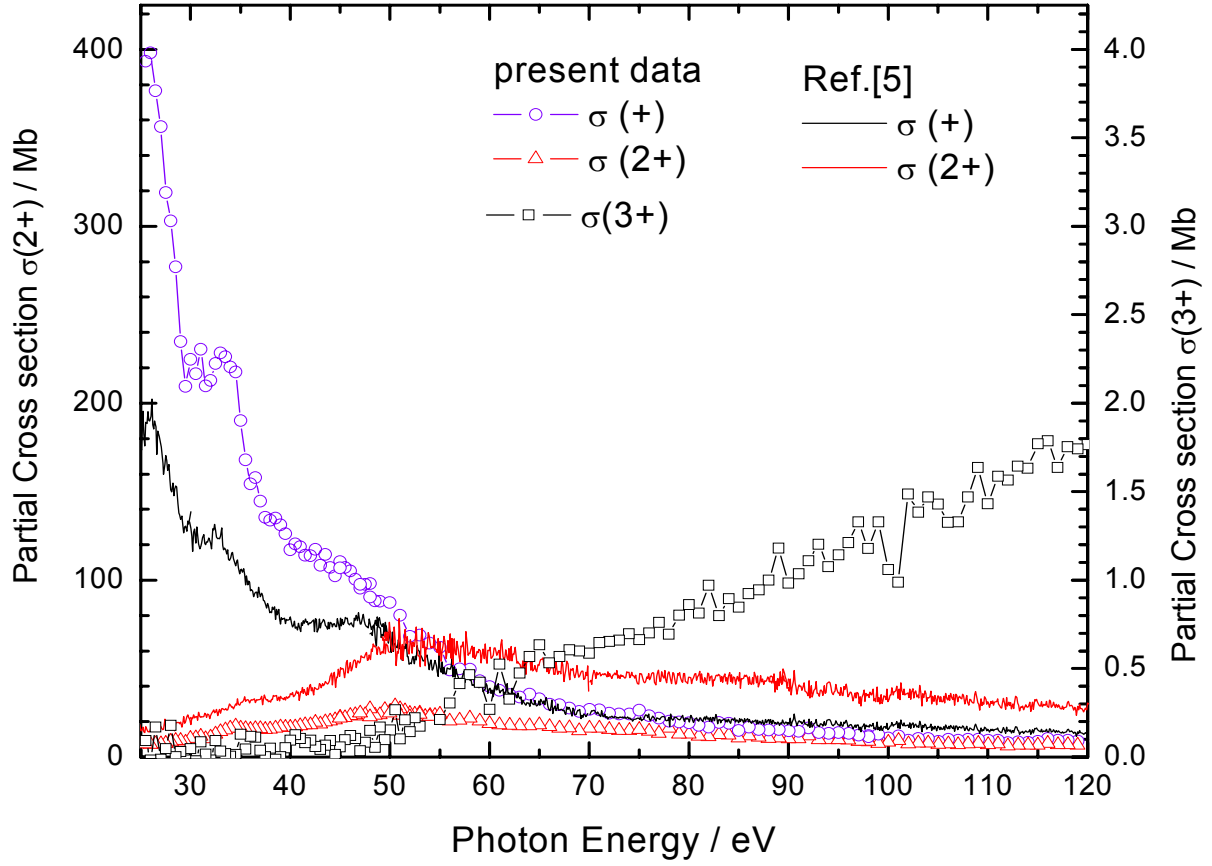


Fig. 4.2. Partial cross sections for single, double and triple photoionization of C_{60} . The open circles, triangles, and squares designate $\sigma_{\text{abs}}(+)$, $\sigma_{\text{abs}}(2+)$, and $\sigma_{\text{abs}}(3+)$, respectively, determined from eq. (1). The solid and dotted curves are $\sigma_{\text{abs}}(+)$ and $\sigma_{\text{abs}}(2+)$, reported by Kou *et al.*, respectively [5]. The two $\sigma_{\text{abs}}(+)$ curves are normalized at $h\nu = 80$ eV.

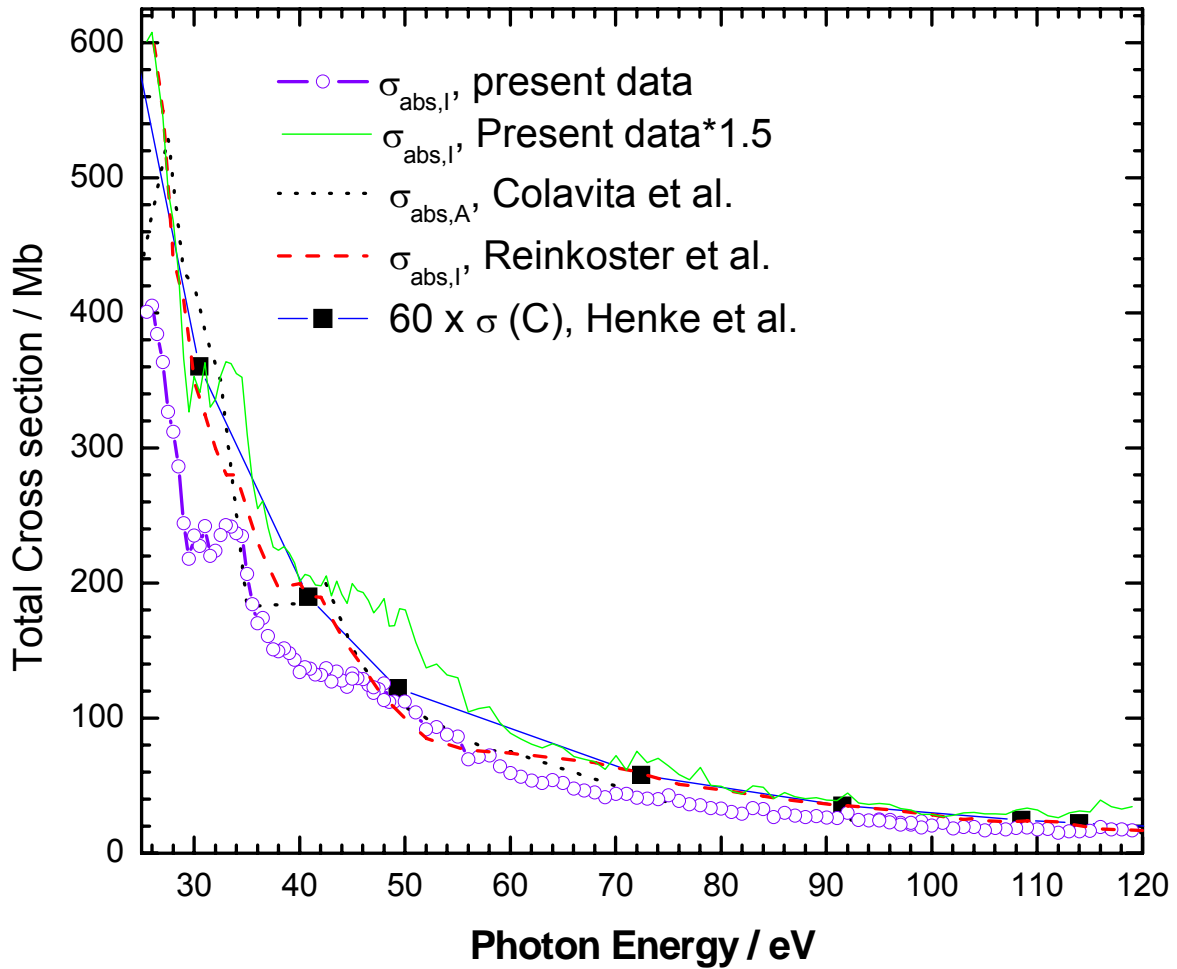


Fig. 4.3. Total photoionization and photoabsorption cross sections of C₆₀. Open circles, $\sigma_{\text{abs,I}}$ of the present study; solid curve, $\sigma_{\text{abs,I}}$ of the present study multiplied by 1.5; dashed curve, experimental $\sigma_{\text{abs,I}}$ by Reinköster *et al.* [6]; the dotted curve, theoretical $\sigma_{\text{abs,A}}$ by Colavita *et al.* [9]; closed squares, 60 times the total photoabsorption cross section [25] of a C atom.

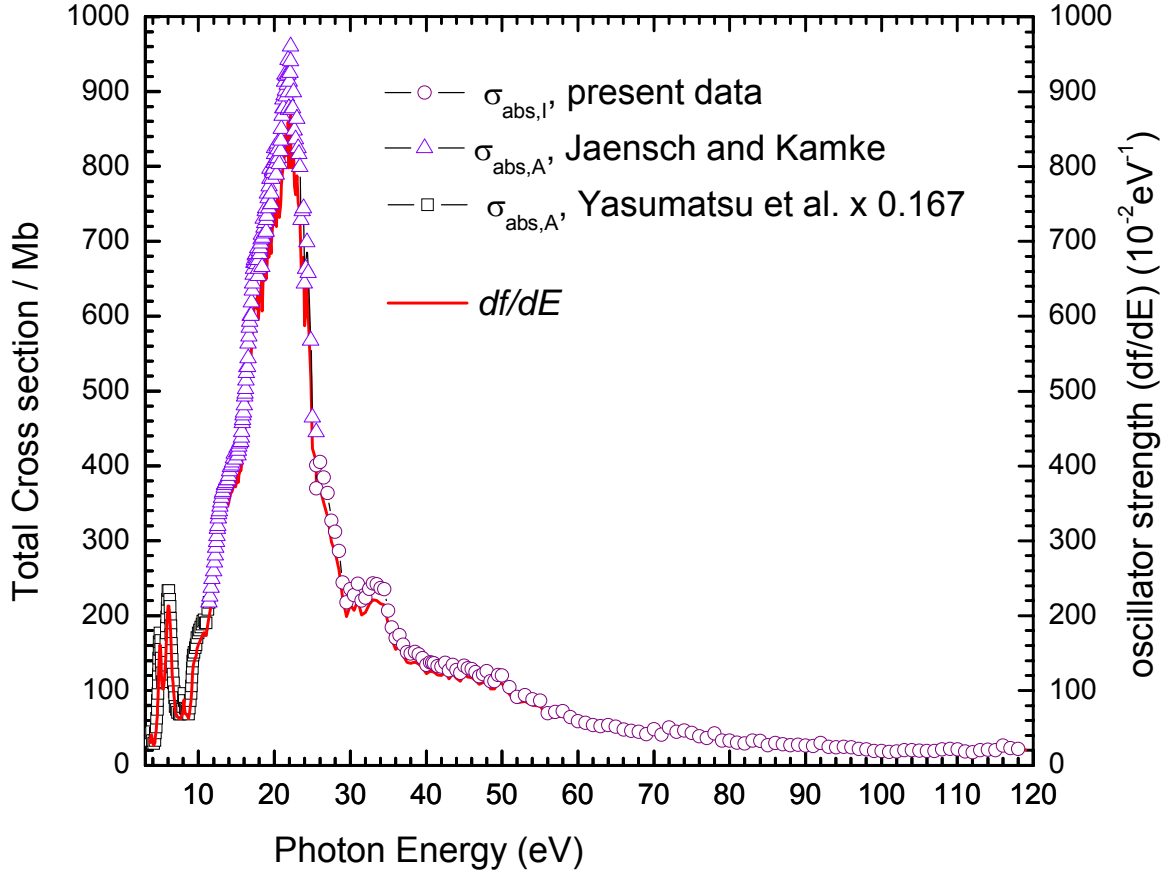


Fig. 4.4. Total photoionization and photoabsorption cross sections of C_{60} in the $h\nu$ range of 3.5 – 119 eV. O, $\sigma_{\text{abs,I}}$ of the present study at 25–119 eV; Δ , $\sigma_{\text{abs,A}}$ given by Jaensch and Kamke [12,13] at 10–25 eV; \square , $\sigma_{\text{abs,A}}$ at 3.5–11eV obtained by dividing the photoabsorption cross sections of Yasumatsu *et al.* [11] by 6. The solid curve denotes the oscillator strength distribution calculated from the above cross sections using eq. (3).

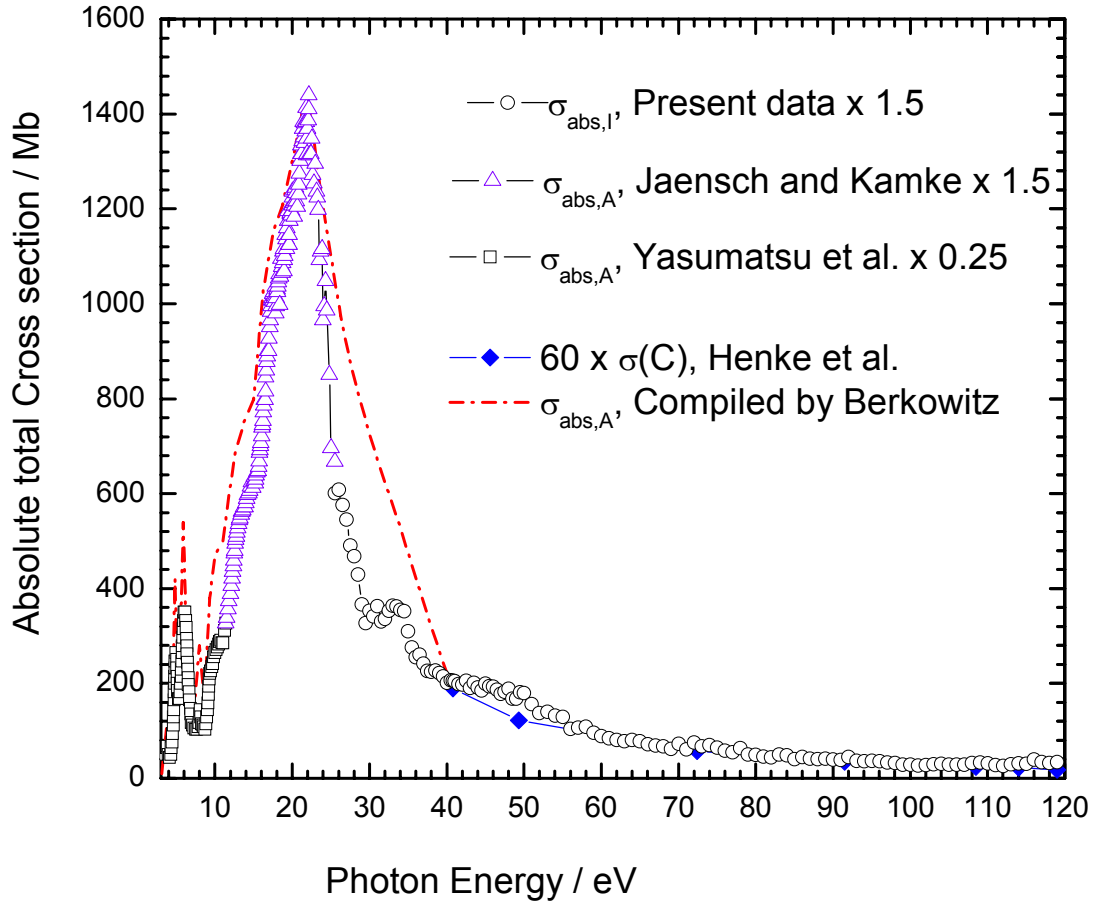


Fig. 4.5. Total photoionization and photoabsorption cross sections of C_{60} in the $h\nu$ range of 3.5–119 eV. This figure is similar to Fig. 4.4, but all the cross sections of C_{60} are reevaluated by using the data of the vapor pressure taken from ref. (21). O, $\sigma_{\text{abs,I}}$ at 25–119 eV obtained by multiplying the photoionization cross sections of the present study by 1.5; Δ , $\sigma_{\text{abs,A}}$ at 10–25 eV obtained by multiplying the photoabsorption cross sections of Jaensch and Kamke [12,13] by 1.5; \square , $\sigma_{\text{abs,A}}$ at 3.5–11 eV obtained by dividing the photoabsorption cross sections of Yasumatsu *et al.* [11] by 4. Closed diamonds represent 60 times the total photoabsorption cross sections of a C atom [25]. The dot-and-dash curve denotes $\sigma_{\text{abs,A}}$ compiled by Berkowitz (ref. 10 and therein).

Chapter 5

Photofragment Imaging Apparatus for Measuring Momentum

Distributions in Dissociative Photoionization of Fullerenes

[AIP Conf. Proc. **879** (2007) 1809]

5.1 Introduction

Much experimental work has been devoted to the study of isolated fullerenes, C_{60} and C_{70} , in the extreme UV region by using energy-controlled electron beam [1-4], synchrotron radiation [5-7], laser [8-11], and fast heavy particles [12,13]. It is well documented that decomposition of nascent C_{60}^{z+} and C_{70}^{z+} formed from C_{60} and C_{70} leads to various carbon clusters C_{60-2n}^{z+} and C_{70-2n}^{z+} ($n \geq 1$, $z \geq 1$) with even-numbered atoms, though dynamical aspects of energy partitioning and fragmentation are not fully elucidated yet. Very recently, dissociative photoionization of C_{60} and C_{70} have been studied by measuring the yield curves of C_{60-2n}^{z+} and C_{70-2n}^{z+} in a wide excitation energy range [5-7]. The behavior of the yield curves can be interpreted in terms of the stepwise mechanism, i.e. internal conversion of the electronically excited states, statistical redistribution of the excess energies among the internal degrees of freedom, and consecutive ejection of C_2 units [6,7]:



There are only a few experimental studies of product analysis of the fragments. The translational energy distribution of C_{60-2n}^+ has been measured by several groups to understand the energetics and mechanism of fragmentation. Hertel and co-workers [8] evaluated the kinetic energies of C_{60-2n}^+ ($1 \leq n \leq 14$) produced by photoionization of C_{60} . Later Märk and co-workers [4] fulfilled electron impact ionization of C_{60} and reported a value of ca. 0.45 eV as the total average kinetic energy release in the

decomposition of C_{60}^+ into C_{60-2n}^+ ($1 \leq n \leq 8$). These authors suggested that not only sequential C_2 ejection of process (1) but also single-step two-fragment fission of the parent C_{60}^+ ions



are possible mechanisms for the formation of C_{60-2n}^+ .

In the present study, I have developed a new version of momentum imaging spectrometer for obtaining reliable velocity distribution of the fullerene fragments. In this chapter a basic design of this spectrometer is described. From photofragment images, one will be able to decide on which mechanism dominates fragmentation of fullerene ions, because three-dimensional velocity distributions are expected to considerably differ for different mechanisms. Moreover, closer inspection of the images may allow us to directly probe the properties of ion states correlated to the dissociation channels. If dissociation channels involve passage over an exit barrier, the distribution of the translational energy in the center of mass system shows a peak at some fraction of the barrier height. In contrast, if little or no exit barrier exists on dissociation channels, the distribution shows peak at close or equal to zero because energy randomization occurs statistically among all the internal degrees of freedom of the parent species [14,15].

Momentum imaging technique was first introduced to the field of molecular reaction dynamics in 1986 by Chandler and Houston [16,17]. In 1997 velocity focusing lens system was invented by Eppink and Parker and a great advance was made in improving the resolution of the image [18]. Using momentum imaging technique photofragmentation processes of fundamental molecules have been studied extensively. In general neutral fragments under study are ionized selectively by resonance-enhanced multiphoton ionization (REMPI) [19] to avoid the interference

from imaging of other fragments. In contrast, it is difficult to obtain clear images of the ionic fragments which are free from contamination of unwanted species. Some authors applied a pulsed high voltage to the front plate of the microchannel plate photomultipliers (MCP) just on the arrival time of the ionic fragments with particular mass-to-charge ratio m/z [20]. However, this method of MCP switching is not so advantageous to large molecules because time of flights of many kinds of fragments are close to one another. Furthermore, application of the pulsed high voltage field brings about distortion of equipotential surface inside a drift tube which reduces the number of ion trajectories reaching the detector. To overcome these difficulties a mass gate and ion reflector was incorporated inside the drift tube of the present photofragment imaging spectrometer, which may provide uncontaminated images of particular ionic fragments from large molecules, clusters, or fullerenes.

5.2 Basic Concept and Design Optimized by Simulations

Figure 5.1 illustrate a schematic design of our spectrometer. All the electrodes and ion drift tube are cylindrically symmetrical. A velocity focusing lens system contains three electrodes: repeller, extractor, and the entrance electrodes of the drift tube. The drift tube is kept grounded throughout the trajectory calculations. Every electrode of the three-element lens system is made of circular plates 1 mm in thickness and 50 mm in outer diameter, separated by 15 mm from each other. The extractor and the entrance electrode of the drift tube have central hole of 20 mm in diameter. Such open-hole structure of the two electrodes allows to bend the equipotential surfaces by simply manipulating the extractor voltage and to achieve the excellent focusing of momentum image on a position sensitive detector PSD which combined with MCP [18,21]. Near the end of the drift tube there are cylindrical *mass gate* and *ion reflector* having the inner diameter of 40 mm. Thin meshes with high transmission are fixed to

both ends of the mass gate in such a way that distortion of equipotential surfaces due to fringe effect is negligibly small. The ion reflector is comprised of three electrodes with fine meshes. Its central electrode is floated to high positive voltage, while the other two electrodes are grounded. The latter electrodes, located 5 mm apart from the central electrode, can keep equipotential surfaces flat and parallel near the reflector. As long as the *mass gate* is set to be ground, all fragments are repelled by *ion reflector* and do not impinge the PSD (effective size = 40 mm). When an entire bunch of the fragments having an expected m/z arrives inside the mass gate, a pulsed voltage is applied there. The potential energies of the ions in this bunch are suddenly elevated so that only the ions inside the *mass gate* can pass through *ion reflector* and reach the PSD.

Ion trajectory simulations were performed utilizing the SIMION 3D (ver. 7.0) software [22] to optimize the dimensions of the electrodes in Fig. 5.1. SIMION makes use of potential arrays that define the geometry and potentials of electrodes and magnetic poles. The potentials of points outside electrodes are determined by solving the Laplace equation by finite difference methods. In SIMION, this process is called *refining* the array. Refined arrays can then be projected as array instances (3D virtual images) into an ion optics workbench volume. Ions can be flown within the workbench volume and their trajectories changed by the fields of the potential array for the instances they fly through.

The grid size of the simulations of 0.5 or 1 mm was adopted to keep a good scale factor. Here, the dissociative ionization of C_{60} is considered to take place within a region of rectangular parallelepiped $\Delta x \Delta y \Delta z = 1 \times 3 \times 1 \text{ mm}^3$ as depicted in Fig. 5.2. The y-coordinate of this region ranges from -1.5 to +1.5 mm because the y-direction is assigned to the passage of synchrotron radiation. In ion trajectory simulations the

eight corners and the center of the ionization region were chosen for the starting points of the trajectories. From each point 171 trajectories were generated in the elevation angular range of -90° to $+90^\circ$ at intervals of 22.5° and in the azimuth angle range of 0° to $+180^\circ$ at intervals of 10° . The definition of the two angles are given in Fig. 5.2. The optimum distance from ionization region to the center of mass gate was 335.5 mm and that to the entrance of the PSD was 360.5 mm. The length of the mass gate (= 10 mm) was so chosen as to accommodate all fragment ions with a particular m/z ratio inside the mass gate. Application of pulsed voltages to repeller and mass gate was realized by means of a “*user program*” of SIMION [22]. The amplitude and duration of the pulsed voltage applied to repeller were 300 V and 7 μs , respectively, and the rising edge of this pulse precede that of the pulsed voltage applied to the mass gate by 44.5 μs . At the mass gate the spread of the time of flight was 0.65 μs which was estimated from the finite volume of the ionization region and the distribution of the kinetic energy of the fragment ions. Thus, the amplitude and duration of the pulsed voltage applied to the mass gate were set to 120 V and 1 μs , respectively. The ratio of applied voltages of extractor to that of repeller was set to be constant at 0.714, while continuous voltage of 320 V was applied to the central electrode of the ion reflector.

5.3 Results

The panel (b) of Figure 5.3 shows simulated trajectories of C_{58}^+ at initial kinetic energy of 0.1 eV, the ion whose momentum image we wish to measure, and panels (a) and (c) present the trajectories of C_{60}^+ and C_{56}^+ , respectively. (The energy 0.1 eV corresponds to the energy of a particular fragment in the laboratory frame of reference including the supplied thermal energy.) Though the trajectories of both C_{60}^+ and C_{56}^+ are reflected completely, most of the trajectories of C_{58}^+ are found to go

beyond the ion reflector and reach the PSD. This result confirms the basic concept in section 5.2 for exclusive imaging detection of C_{58}^+ by excluding C_{60}^+ and C_{56}^+ with same kinetic energies.

Moreover, a linear dependence between (quasi-linear relation) between the y-component of the momentum (P_y) and that of the displacement on PSD (Δy) is obtained as shown in the Fig. 5.4a. A similar trend was also observed between the x-component of the momentum (P_x) and the time of flight difference of ions Δt ($\Delta t = t_0 - t$) to reach the PSD (Fig. 5.4b). Here, t and t_0 are the time-of-flight of ions with and without certain amount of initial kinetic energy, respectively. These observations allow to transform the displacement of ionic fragment on PSD to obtain velocity and spatial distribution of a desired fragment.

Figure 5.5 shows the image of C_{58}^+ ions on the PSD at the kinetic energy of 0.1 eV (triangles) and 0.11 eV (circles). We took into account the ion trajectories generated in the elevation and azimuth angles in the ranges of 0° to $+90^\circ$ and 0° to $+180^\circ$, respectively, which cover one quarter of the full three-dimensional trajectories over the 4π solid angle. The trajectories with a given elevation angle form a horizontal stripe, and the envelope of all the stripes makes an arc, which clearly demonstrates that angular distribution in spherical symmetry can be successfully projected on an image plane. It is likely that C_{58}^+ fragment ions with kinetic energy difference of 0.01 eV are almost separable. Comparison between the simulations with and without the ion reflector confirmed that the images are not distorted in the presence of the ion reflector. The present momentum imaging spectrometer has already been constructed and installed at the end station of beam line 2B in the UVSOR facility.

5.4 Conclusions

In the present study, a photofragment imaging apparatus has been developed based on time-of-flight (TOF) mass spectrometry to measure the kinetic energy and angular distributions of the fragments.

The Eppink–Parker type three-element velocity focusing lens system (electrodes R, E, and T) has been adopted to achieve high kinetic energy resolution on the photofragment images. Furthermore, a potential switchable mass gate and an ion reflector inside the TOF tube were utilized to select a bunch of fragments having the same mass-to-charge ratio m/z from neighboring bunches $(m \pm 24)/z$. Results obtained by ion trajectory simulations, using the SIMION 3D software, confirms the basic concept for exclusive imaging detection of a desired ionic fragment produced from C_{60} (for e.g. C_{58}^+ ions which are produced from parent C_{60} molecules) after excluding unwanted fragments (for e.g. C_{60}^+ and C_{56}^+) with the same kinetic energies

Moreover, a linear dependence between (quasi-linear relation) between the y-component of the momentum (P_y) and that of the displacement on PSD (Δy) is obtained. This observation allows one to transform the displacement of ionic fragment on PSD to obtain velocity and spatial distribution of a desired fragment.

The simulated image of C_{58}^+ ions on the PSD at the different kinetic energies of 0.1eV and 0.11eV show that the trajectories with a given elevation angle form a horizontal stripe, and the envelope of all the stripes makes an arc, which clearly demonstrates that angular distribution in spherical symmetry can be successfully projected on an image plane. It is likely that C_{58}^+ fragment ions with kinetic energy difference of 0.01 eV are almost separable. The present momentum imaging spectrometer has been constructed and installed in the end station of beam line 2B in the UVSOR facility. The preliminary experimental results obtained using Kr sample

show that ions produced in the ionization region can be focused at the center of the PSD (within 2mm), if image defocusing due to thermal energy of the molecule is omitted.

The present momentum imaging spectrometer will be utilized to obtain reliable velocity distributions of the fullerene fragments. From photofragment images, we will be able to decide on which mechanism dominates fragmentation of fullerene ions, since three-dimensional velocity distributions are expected to considerably differ for different mechanisms.

References:

- [1] M. Foltin, M. Lezius, P. Scheier, and T. D. Märk, *J. Chem. Phys.* **98** (1993) 9624.
- [2] P. Scheier, B. Dünser, R. Wörgötter, M. Lezius, R. Robl, and T. D. Märk, *Int. J. Mass. Spectrom. Ion Proc.* **138** (1994) 77.
- [3] S. Matt, B. Dunser, M. Lezius, H. Deutsch, K. Becker, A. Stamatovic, P. Scheier and T. D. Märk, *J. Chem. Phys.* **108** (1998) 963.
- [4] D. Muigg, G. Denifl, P. Scheier, K. Becker, and T. D. Mark, *J. Chem. Phys.* **108** (1998) 963.
- [5] A. Reinköster, S. Korica, G. Prümper, J. Viefhaus, K. Godehusen, O. Schwarzkopf, M. Mast, and U. Becker, *J. Phys. B: At. Mol. Opt. Phys.* **37** (2004) 2135.
- [6] J. Kou, T. Mori, Y. Kubozono, and K. Mitsuke, *Phys. Chem. Chem. Phys.* **7** (2005) 119.
- [7] K. Mitsuke, H. Katayanagi, J. Kou, T. Mori, and Y. Kubozono, *Am. Inst. Phys. CP* **811** (2006) 161.
- [8] H. Gaber, R. Hiss, H. G. Busmann, and I. V. Hertel, *Z. Phys. D* **24** (1992) 307.
- [9] P. Wurz and K. R. Lykke, *J. Phys. Chem.* **96** (1992) 10129.
- [10] D. Ding, R. N. Compton, R. E. Haufler, and C. E. Klots, *J. Phys. Chem.* **97** (1993) 2500.
- [11] J. Laskin, B. Hadas, T. D. Märk, and C. Lifshitz, *Int. J. Mass Spectrom.* **177** (1998) L9.
- [12] B. Walch, C. L. Cocke, R. Voelpel, and E. Salzborn, *Phys. Rev. Lett.* **72** (1994) 1439.
- [13] T. LeBrun, H. G. Berry, S. Cheng, R. W. Dunford, H. Esbensen, D. S. Gemmell, E. P. Kanter, and W. Bauer, *Phys. Rev. Lett.* **72** (1994) 3965.

- [14] D. H. Mordaunt, D. L. Osborn, and D. M. Neumark, *J. Chem. Phys.* **108** (1998) 2448.
- [15] A. E. Faulhaber, D. E. Szpunar, K. E. Kautzman, and D. M. Neumark, *J. Phys. Chem. A* **109** (2005)10239.
- [16] D.W. Chandler and P. L. Houston, *J. Chem. Phys.* **87** (1987) 1445.
- [17] P. L. Houston, *J. Phys. Chem.* **100** (1996)12757.
- [18] A. T. J. B. Eppink and D. H. Parker, *Rev. Sci. Instrum.* **68** (1997) 3477.
- [19] M. Ito and M. Fuji, “ *Advances in Multi-Photon Processes and Spectroscopy,* ” ed. S. H. Lin, Word Scientific (Singapore, 1988) Vol. 4, p.1-68.
- [20] F. Aguirre and S. T. Pratt, *J. Chem. Phys.* **118** (2003) 6318.
- [21] B. Tang and B. Zhang, *Chem. Phys. Lett.* **412** (2005) 145.
- [22] D. A. Dahl, SIMION 3D 7.0, Boise Idaho: Scientific Instrument Services Inc. 2000.

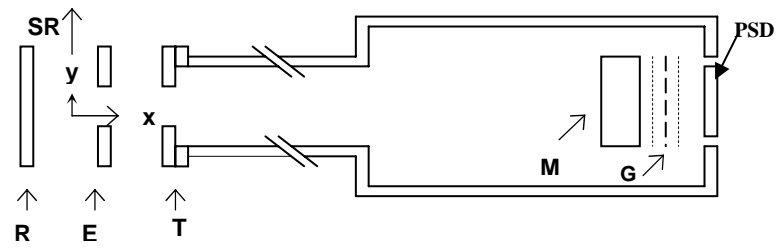


Figure 5.1. Schematic view of the momentum imaging spectrometer in combination with the mass gate M and ion reflector G. The dimensions of all the electrodes are determined from the SIMION 3D software. R, Repeller; E, extractor; T, Entrance electrode of a drift tube; SR, synchrotron radiation.

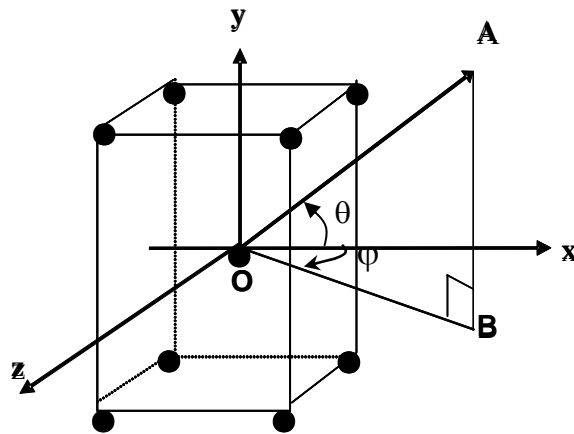


Figure 5.2. Ionization volume and coordinate system defined for simulations. OA, ion emission direction; OB, projection of OA on the x-z plane; θ , elevation angle; φ , azimuth angle.

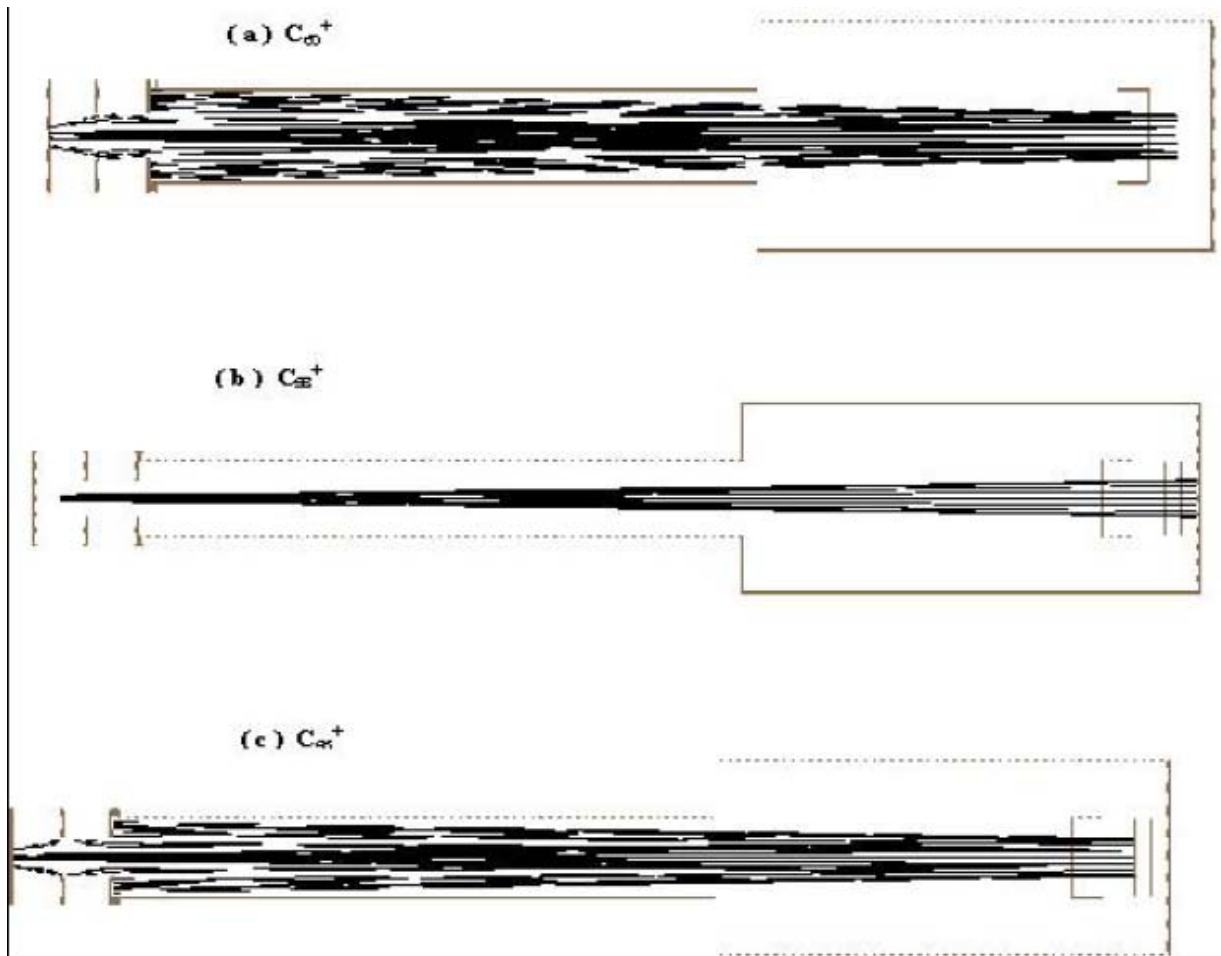


Figure 5.3. Simulated trajectories of (a) C_{60}^+ , (b) C_{58}^+ , (c) C_{56}^+ at initial kinetic energies of 0.1 eV. The trajectories of C_{60}^+ and C_{56}^+ are found to turn around at the ion reflector, travel in the opposite direction and terminate at repeller electrode.

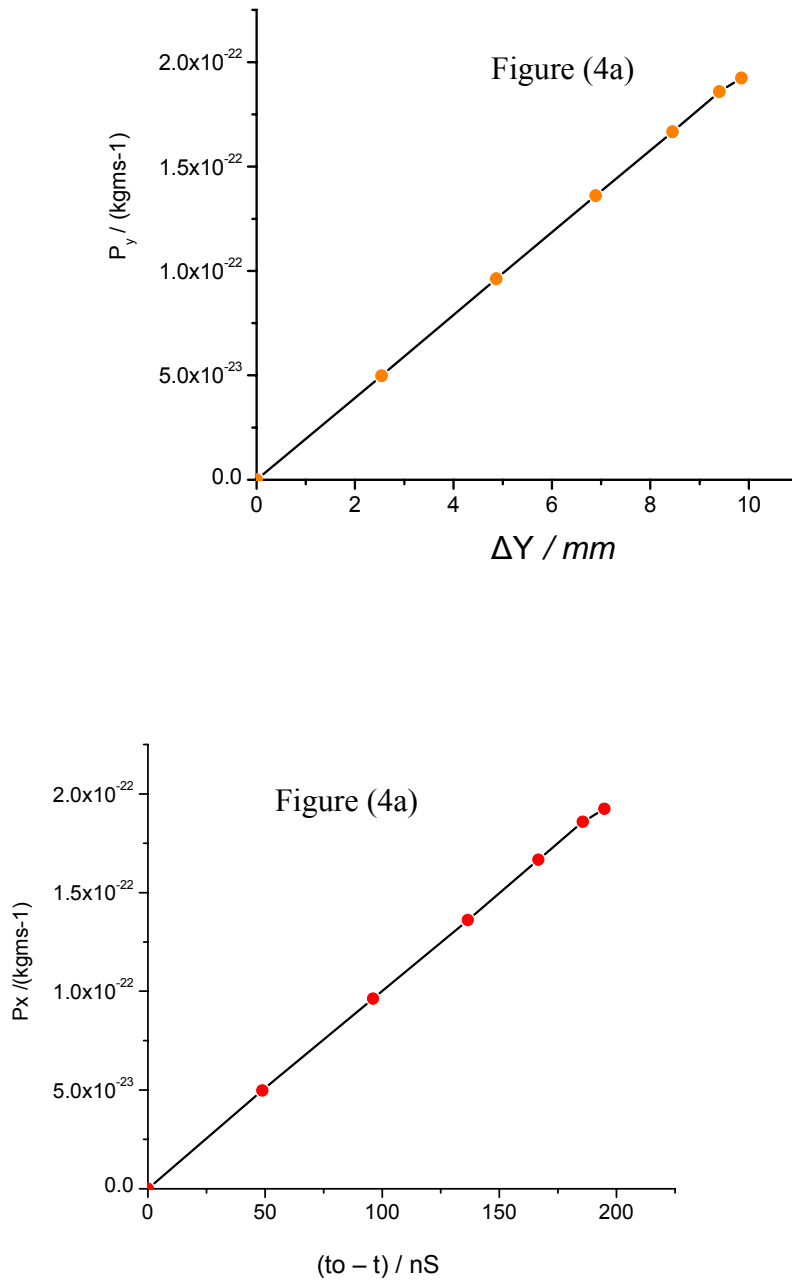


Fig. 5.4 (a), quasi-linear relationship between the y-component of the momentum (P_y) and that of the displacement at PSD; Fig. (4b), x-component of the momentum (P_x) and difference in time of flight of ions Δt ($\Delta t = t_0 - t$) to reach the PSD (see text). Trajectories from ionization region are ejected by ejection angle of every 15° from angle $0 - 90^\circ$.

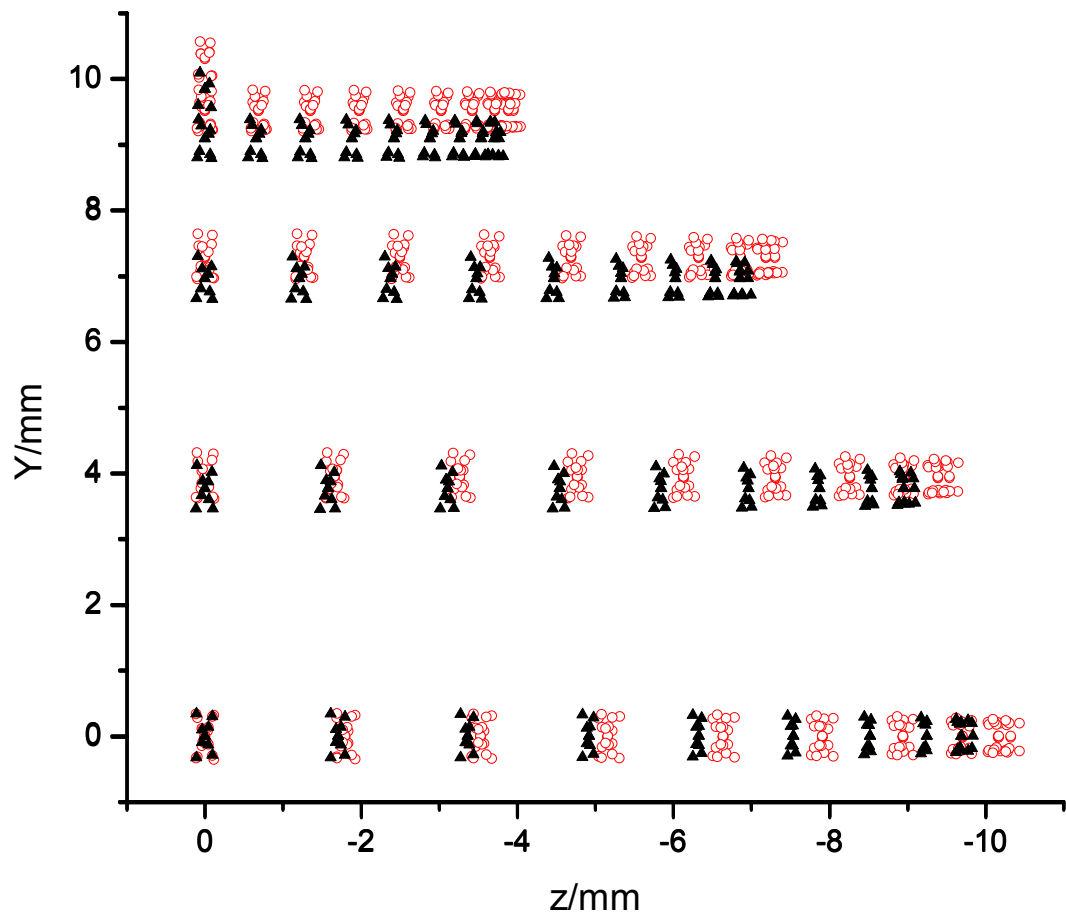


Figure 5.5. Projection of three-dimensional angular distribution of C_{58}^+ ions on the PSD at the initial kinetic energies of 0.1 (\blacktriangle) and 0.11 eV (\circ).

Chapter 6

Summary of the Thesis

This chapter summarizes the two major works of this thesis:

(I) the determination of absolute total photoionization cross section of C_{60} excited with synchrotron radiation in the extreme UV region from 25 to 120 eV described in chapter four and

(II) the new design of the photofragment imaging apparatus for measuring momentum distributions of cationic fragments produced after photodissociation of C_{60} described in the chapter five.

The absolute partial cross sections for single double and triple photoionization of C_{60} in the energy range from 25 to 120 eV was experimentally determined using tunable synchrotron radiation. Precise evaluation of the absolute detection efficiency of our TOF spectrometer, fraction of the second-order light, and the vapor pressure of C_{60} above 700 K allowed us to obtain the most reliable absolute total photoionization cross sections of C_{60} . Particularly, these results directed us that correction of the detection efficiencies is critical to obtain accurate partial cross sections of highly polyatomic and multiply bonded molecules such as C_{60} .

The oscillator strength f was calculated, by combining the present cross sections $\sigma_{\text{abs,I}}$ with the $\sigma_{\text{abs,A}}$ data measured by Jaensch and Kamke ($h\nu = 11.4\text{--}25$ eV) [1,2], and Yasumatsu *et al.* ($h\nu = 3.5\text{--}11.4$ eV) [3]. However, these f (the obtained values were 120.4 and 156.0, respectively, for the $h\nu$ ranges from 3.5 to 40.8 eV and from 3.5 to 119 eV) values were significantly smaller than the corresponding oscillator strengths of 187.6 and 233.4 expected from the TKR sum rule and $60 \times \sigma(C)$ [4]. The insufficiency of f is entirely predictable because the $\sigma_{\text{abs,A}}$ data points of

Jaensch and Kamke [1,2], who conceivably overestimated the vapor pressure of C₆₀, lie much below than those compiled by Berkowitz [4]. By using the vapor pressure data of Piacente *et al.*, reevaluation of the absorption cross section data $\sigma_{\text{abs,A}}$ of Yasumatsu *et al.* [3] and of Jaensch and Kamke [1,2] was made. Then the oscillator strengths was recomputed and achieved the values to be 178.5 and 230.5 for the $h\nu$ ranges from 3.5 to 40.8 eV and from 3.5 to 119 eV, respectively. These values agree well with the oscillator strength expected from the TKR sum rule and $60 \times \sigma(\text{C})$, namely 187.6 and 233.4, respectively. I therefore conclude that the absolute photoabsorption cross section curve in Fig. 4.5 is more plausible than that in Fig. 4.4 in chapter four of this thesis.

Actually, Berkowitz has compiled the absorption spectrum of C₆₀ using all available experimental data by that time (noticeably, above 40.8 eV, the spectrum derived by him was mainly from $60 \times \text{C}$ atom cross section). However, in the discussion based on sum rules, a reduction of the cross section of about 22 % was proposed to improve agreement with TKR sum rule. Furthermore, Berkowitz also stressed the necessity of further study from 11- 40 eV domain in order to clarify not only the absolute cross section values but also the shapes and widths of peaks in this energy region. I believe that the improved curve (fig. 4.5) from present study definitely represents more reliable curve and clarifies the shape and widths of the peaks. As ab initio calculations of a system as large as C₆₀ are difficult to perform with accuracy, spectrum from present study will provide an excellent opportunity for comparing the theoretically calculated cross sections of C₆₀.

In the chapter five, I have reviewed on the possible dissociation processes of highly excited C₆₀ molecule, when it is exposed to a photon of energy ~ 41 eV or above, and discussed regarding unsolved problems of product analysis of the

fragments. Then, in the present study, a photofragment imaging apparatus has been developed based on time-of-flight (TOF) mass spectrometry (adopting Eppink–Parker type three-element velocity focusing lens system [5]) in order to measure the kinetic energy and angular distributions of the fragments produced from C_{60} . To select a bunch of fragments having the same mass-to-charge ratio (m/z) from neighboring bunches $(m \pm 24)/z$, for example, to separate C_{58}^+ from C_{60}^+ and C_{56}^+ , a potential switchable *mass gate* and an *ion reflector* were utilized.

Results obtained by ion trajectory simulations, using the SIMION, confirms the basic concept for exclusive imaging detection of a desired ionic fragment produced from C_{60} (for e.g. C_{58}^+ ions which are produced from parent C_{60} molecules) after excluding unwanted fragments (for e.g. C_{60}^+ and C_{56}^+) with the same kinetic energies.

Moreover, a linear dependence between (quasi-linear relation) between the y -component of the momentum (P_y) and that of the displacement on PSD (Δy) is obtained. This observation allows one to transform the displacement of ionic fragment on PSD to obtain velocity and spatial distribution of a desired fragment.

The simulated images of C_{58}^+ ions on the PSD at the different kinetic energies of 0.1eV and 0.11eV show that C_{58}^+ fragment ions with kinetic energy difference of 0.01 eV are almost separable. The preliminary experimental results using the present momentum imaging spectrometer (installed in the end station of beam line 2B in the UVSOR facility) on Kr sample at room temperature (Kr^+ and Kr^{2+} were focused on to the PSD) show that ions produced in the ionization region can be focused at the center of the PSD (within 2mm), if image defocusing due to thermal energy of the molecule is omitted. This experimentally observed result guides us that one of the objectives of the present design is fulfilled. Thus, present momentum imaging spectrometer can be utilized to obtain reliable velocity distributions (and also translational energy

distribution) of the fullerene fragments. From photofragment images, one will be able to decide on which mechanism dominates fragmentation of fullerene ions between sequential loss of C₂ unit ($C_{60-2n+2}^{z+} \rightarrow C_{60-2n}^{+} + C_2$) and single-step two-fragment fission ($C_{60}^{+} \rightarrow C_{60-2n}^{+} + C_{2n}$) of the parent C₆₀⁺ ions. Because three-dimensional velocity distributions are expected to considerably differ for different mechanisms.

References

- [1] R. Jaensch and W. Kamke, *Mol. Mater.* **13** (2000) 143.
- [2] W. Kamke, private communication, revised data of ref. 12.
- [3] H. Yasumatsu, T. Kondow, H. Kitagawa, K. Tabayashi, and K. Shobatake, *J. Chem. Phys.* **104** (1996) 899.
- [4] J. Berkowitz, *J. Chem. Phys.* **111** (1999) 1446.
- [5] A. T. J. B. Eppink and D. H. Parker, *Rev. Sci. Instrum.* **68**, 3477-3484 (1997).

Appendixes

Appendix 1

Absolute partial cross sections $\sigma_{\text{abs}}(z^+)$ for the formation of $\text{C}_{60}^{z^+}$ from C_{60} can be calculated from the summed count rate R of the ion signal of $\text{C}_{60}^{z^+}$. Particularly $\sigma_{\text{abs}}(z^+)$ can be written as:

$$\sigma_{\text{abs}}(z^+) = \frac{R(z^+)}{\Phi n L F \tau} \cdot \frac{1}{\eta_{\text{abs}}(\text{C}_{60}^{z^+})} \quad (1a)$$

Here, $R(z^+)$ is the signal count rate of the photoions in a charge state z , Φ is the photon flux of synchrotron radiation, n is the number density of C_{60} in the ionization region, L is the length of the ionization volume along the light path, F is the repetition rate of the pulsed electric field, τ is the average residence time of the ions in the ionization volume under the field free condition, $\eta_{\text{abs}}(\text{C}_{60}^{z^+})$ is the absolute overall detection efficiency of the apparatus for $\text{C}_{60}^{z^+}$. For C_{60} , n is proportional to the mass deposition rate D of the thickness monitor and to the inverse of the average flow speed of the neutral C_{60} beam at the oven temperature, T . Assuming effusive flow conditions through the conical nozzle [1-4], the average flow speed \bar{v} can be approximated by the velocity component vertical to the light path as:

$$\bar{v} = \frac{1}{2} \sqrt{\frac{8k_B T}{\pi m}} \quad (1.1)$$

where k_B is the Boltzmann constant and m is the mass of C_{60} . Then the sample number density n is given by:

$$n = \frac{DS_1}{s_2 \bar{v} m A} \quad (1.2)$$

where D is the mass deposition rate of the thickness monitor, S_1 and S_2 are, respectively, the circular cross sections of the molecular beam at the thickness monitor and the light path and A is the effective area of the thickness monitor.

Substituting the values of \bar{v} , n and $\tau\left(=\frac{l}{\bar{v}}\right)$ in the eq. (1a) we obtain,

$$\sigma_{abs}(z+) = \frac{2R(z+)AS_2k_B T}{\pi\Phi Ll FDS_1} \cdot \frac{1}{\eta_{abs}(C_{60}^{z+})} \quad (1b)$$

where l is the length of ionization volume along the molecular beam path.

References:

- [1] R. Jaensch and W. Kamke, *Mol. Mater.* **13** (2000) 143.
- [2] T. Mori, J. Kou, Y. Haruyama, Y. Kubozono, and K. Mitsuke, *J. Electron Spectrosc. Relat. Phenom.* **144-147** (2005) 243.
- [3] J. Abrefah, D. R. Olander, M. Balooch, and W. J. Siekhaus, *Appl. Phys. Lett.* **60** (1992) 1313.
- [4] V. Piacente, G. Gigli, P. Scardala, A. Giustini, and D. Ferro, *J. Phys. Chem.* **99** (1995) 14052.

Appendix 2

Photoabsorption and Oscillator strength

If an electron bound to a nuclear framework possessed perfect oscillating properties following harmonic motion, then according to classical theory the excitation probability of this electron would be said to have an *oscillator strength* (f) of unity. The concept of the optical oscillator strength has been developed for providing a useful measure of the transition probability [1-3].

In classical model, electrons are envisaged as bound to their equilibrium position by a restoring force proportional to their displacement $x(t)$ at time t , and thus undergoing harmonic oscillation at natural (angular) frequency (w_n). The restoring force is due to all other constituents of matter (viz., other electrons and nucleus), which also cause energy losses from electron motion. Its overall effect may be schematically represented by frictional force proportional to the speed $dx(t)/dt$ with a small damping coefficient (g_n). Suppose that there is a light wave, represented by an external electric field of unit strength and angular frequency (w), viz., $E(t) = E_o \exp^{-iwt}$. Here, $E(t)$ is assumed to be independent of the spatial position, i.e., all parts of the atom or molecule experiences the same electric field. (In contemporary words, according to Inokuti [2], it is nothing but the dipole approximation which holds so long as the wavelength of the electromagnetic wave is much greater than the linear dimension of the electron orbit.) Then, the Newton equation of motion for an electron is

$$m \frac{d^2 x(t)}{dt^2} = -mw_n^2 x(t) - mg_n \frac{dx(t)}{dt} - E_o e^{-iwt} \quad (2.5)$$

For which solution is

$$x = \frac{e}{m} \left(\frac{e^{-iwt}}{w_s^2 - w - ig_s w} \right) \quad (2.6)$$

The polarizability α of a system is defined as the dipole moment induced by unit electric field strength, i.e., α per electron = α_I

$$\alpha_1 = \frac{\mu}{E_o e^{-i\omega t}} = \frac{ex}{E_o e^{-i\omega t}} = \frac{e^2}{m} \left(\frac{1}{\omega_s^2 - \omega - ig_s \omega} \right) \quad (2.7)$$

If we have f_s oscillators (electrons) of frequency ω_s , then the polarizability per atom (or molecule) is

$$\alpha_N = \frac{e^2}{m} \sum_s \left(\frac{f_s}{\omega_s^2 - \omega - ig_s \omega} \right) \quad (2.8)$$

As the notion of the oscillator strength is originally due to Thomson. In his theory, f_s , ω_s , and g_s are empirical parameters. Later Heisenberg and Kramers derived the same expression from quantum mechanics, as summarized by Fano and Cooper [3]. Quantum Mechanically, one must consider the mean value of the displacement \bar{x} (or equivalently, the mean value of the induced dipole moment $e\bar{x}$) when an external field is imposed upon an atomic or molecular system. More importantly, they give the prescription for evaluating f_s , ω_s , and g_s . In particular,

$$f_s = \left(\frac{2m\omega_s}{3\hbar} \right) \left| \langle s | \sum_j x_j | 0 \rangle \right|^2 \quad (2.9)$$

is expressed in terms of the dipole matrix element squared $\left| \langle s | \sum_j x_j | 0 \rangle \right|^2$ between the ground state 0 and the excited state s.

References

1. J. Berkowitz, In: *Photoabsorption, Photoionization, and Photoelectron Spectroscopy* Academic Press, New York, 1979 p. 59.
2. M. Inokuti, *Photochem. Photobiol.* **44** (1986) 279.
3. U. Fano, and J. W. Cooper, *Rev. Mod. Phys.* **40** (1968) 441.

List of Publications

(1) “Absolute Total Photoionization Cross Section of C₆₀ in the Range of 25 to 120 eV, Revisited”, **B. P. Kafle**, H. Katayanagi, S. I. Prodhan, H. Yagi, C. Huang, and K. Mitsuke, *J. Phys. Soc. Jpn.*, in press.

(2) “Photofragment Imaging Apparatus for Measuring Momentum Distributions in Dissociative Photoionization of Fullerenes”,

Bhim P. Kafle, Hideki Katayanagi, and Koichiro Mitsuke, *AIP Conf. Proc.* 879 (2007) 1809.

(3) “Relative Partial Cross Sections for Single, Double, and Triple Photoionization of C₆₀ and C₇₀”, K. Mitsuke, H. Katayanagi, **B. P. Kafle**, C. Huang, H. Yagi, Md. S. I. Prodhan, and Y. Kubozono, *J. Phys. Chem. A*, 111 (2007) 8336.

(4) “The 4d - 4f dipole resonance of the Pr atom in an endohedral metallofullerene, Pr@C82”,

Hideki Katayanagi, **Bhim P. Kafle**, Junkei Kou, Takanori Mori, Koichiro Mitsuke, Yasuhiro Takabayashi, Eiji Kuwahara and Yoshihiro Kubojono, *J. Quant. Spectrosc. Radiat. Transfer*, accepted.

(5) “Analytical Model of Electrodiffusion of Metals in Fullerene Thin Films”

Bhim P. Kafle, Isaak Rubinstein and Eugene A. Katz, *Jpn. J. Appl. Phys.* **44** (2005) 2803.